Simulations of Gasotransmitter Permeation Through Lipid Bilayers

by

© **Fatemehsadat Sajadi**

A thesis submitted to the School of Graduate Studies in partial fulfillment of the requirements for the degree of Master of Science.

Department of Chemistry

Memorial University of Newfoundland

October 2018

St. John's, Newfoundland and Labrador, Canada

Abstract

The permeation of gasotransmitter molecules, NO, CO and H_2S, through phospholipid bilayers were studied using molecular dynamics simulations in order to gain insight into the process by which these solutes cross biological membranes. These simulations require accurate representations of both lipids and water components of the simulation. The CHARMM36 lipid model is generally effective at predicting the properties of lipid bilayers, but this model was developed for use with CHARMM TIP3P water model. This water model overestimates the dielectric constant and diffusion coefficient of water, which introduces error into the permeability calculations. The TIP3P-FB and TIP4P-FB water models are more accurate in predicting the dielectric constant and transport properties of water, which could allow for more realistic simulations of membrane permeation. To validate whether these water models are compatible with the CHARMM36 lipid model, the lipid headgroup area, compressibility, order parameters, and scattering form factors were calculated using these models and were generally found to be in good agreement with the experimental values. This indicates that the CHARMM36 model can be used with either of these water models without modification. Using the TIP4P-FB water model and the CHARMM36 lipid force field, the permeation of NO, CO, and H_2S through a POPC lipid bilayer was simulated. These simulations show that the Gibbs energy barriers to permeation are modest for all three gasotransmitters, allowing them to permeate membranes readily. High rates of permeation for NO and H_2S were calculated using the inhomogeneous solubility–diffusion model, in good agreement with experiments. Although no experimental value has been reported, the rate of CO permeation was found to be similar to that of NO. The effect of cholesterol content in the bilayer was also investigated and was found to lower the rates of permeation modestly.

Acknowledgements

I would like to thank my supervisor Dr. Christopher Rowley for his great support and guidance. I would like to thank NSERC of Canada for funding through the Discovery Grants program. I would also like to thank the School of Graduate Studies at Memorial University for a graduate fellowship and Dr. Liqin Chen for a scholarship. Computational resources were provided by Compute Canada and by the Center for Health Informatics and Analytics (CHIA) of the Faculty of Medicine of Memorial University of Newfoundland. I would also like to thank Dr. Norbert Kučerka for providing the X-ray and neutron scattering data using in Chapter 2.

Statement of Contribution

I was responsible for carrying out simulations and writing scripts to analyze the data in Chapter 2 and 3. I was also responsible for making the figures for Chapter 2 and 3. I wrote the manuscripts in collaboration with the co-authors.

Table of Contents

List of Tables

List of Figures

List of Symbols

A_L	lipid headgroup area
K_A	lipid surface area compressibility
J	flux
ΔC	concentration gradient
P_m	permeability coefficient
δt	timestep
v	velocity
q	atomic charge
ρ	electron density distribution
ϕ	membrane dipole potential
L	length of simulation cell
n_L	number of lipids per leaflet
k_B	Boltzmann constant
T	temperature
ζ	electrostatic potential
ΔG	relative Gibbs energy
P_m	permeability coefficient
D	diffusivity
ρ_w	number density of liquid water
η	viscosity coefficient
$\Delta\mu$	excess chemical potential
R_{min}	distance at which the Lennard-Jones potential reaches its minimum
σ	Lennard-Jones radii
ϵ	Lennard-Jones well depth
ΔG_{solv}	Gibbs energy of solvation
R	gas constant

List of Abbreviations

AIMD	*ab initio* molecular dynamics
CHARMM	Chemistry at HARvard Macromolecular Mechanics
DPPC	1,2-dipalmitoyl-sn-glycero-3-phosphocholine
EPR	Electron Paramagnetic Resonance
FB	ForceBalance
GROMACS	GROningen MAchine for Chemical Simulations
GROMOS	GROningen MOlecular Simulation
MD	Molecular Dynamics
MDP	Membrane Dipole Potential
NAMD	Nanoscale Molecular Dynamics
NIST	National Institute of Standard and Technology
NMR	Nuclear Magnetic Resonance
NSL	Neutron Scattering Length
NSLD	Neutron Scattering Length Density
NpT	Isothermal-isobaric ensemble
NVT	Isothermal-isochoric ensemble
mTIP3P	Modified version of TIP3P
OPC	Optimal Point Charge
PME	Particle Mesh Ewald
POPC	1-palmitoyl-2-oleoyl-sn-glycero-3-phosphocholine
RDF	Radial Distribution Function
SPC	Simple Point-Charge water model
SPC/E	Extended Simple Point Charge water model
TI/FEP	Thermodynamic Integration / Free Energy Perturbation
TIP3P	Transferable Intermolecular Potential with 3 Points
VMD	Visual Molecular Dynamics
WHAM	Weighted Histogram Analysis Method

Chapter 1

Introduction

Biological cells and the organelles within these cells are separated from their environments by thin membranes. These membranes are largely composed of amphiphilic lipid molecules, which contain a hydrophilic head group linked to hydrophobic tail groups. The most abundant types of biological lipids are phospholipids, which have a phosphate-containing head group linked to two linear fatty-acid-derived tail groups through a glycerol-derived group. These lipids self-assemble to form a bilayer-structure composed of an upper and lower leaflet. The polar head groups of each leaflet face the solution, while the tail groups of each leaflet form a fluid membrane interior with properties that are similar to long-chain alkane fluids in some respects. A schematic lipid bilayer is shown in Figure 1.1. Refs. [1] and [2] provide a more detailed discussion of elementary membrane physiology.

1.0.1 Chemical Composition and Nomenclature of Lipids

A wide variety of lipids are present in biological membranes. The chemical composition of the headgroup, linkage, and tail groups can all vary. Phosphocholine, where the phosphate group is bound to a $-\mathrm{N}(\mathrm{CH}_3)_3{}^+$ group, is one of the most common

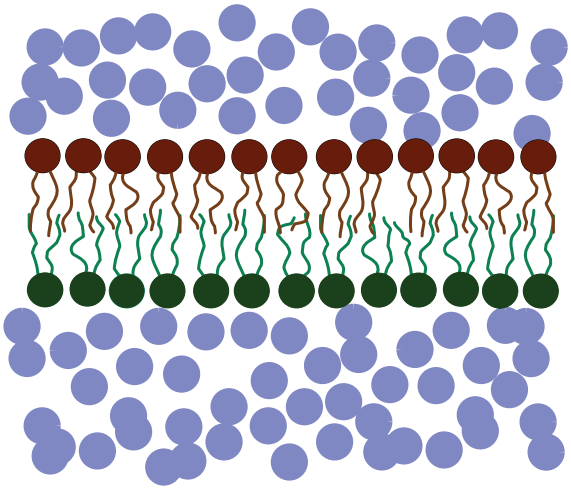

Figure 1.1: Schematic lipid bilayer. The water solution is represented by blue circles. Lipid headgroups are shown as circles and the lipid tails are the lines extending from these circles. The upper leaflet is shown in red and the lower leaflet is shown in green. This figure is adapted with permission from Ref. [3].

types of lipid headgroups. The lipid tails can also vary in length and by partial unsaturation of the chain. In addition to various phospholipids, membranes also contain other components, including cholesterol and membrane proteins [4].

The complex composition of real membranes has led to the practice of developing simpler membranes to serve as models [5]. Some of these model bilayers contain only a single type of lipid that is considered representative of the membrane [6]. Popular model membranes include 1,2-dipalmitoyl-sn-glycero-3-phosphocholine (DPPC) and 1-palmitoyl-2-oleoyl-sn-glycero-3-phosphocholine (POPC). Other model membranes are more complex due to the inclusion of a second component, like cholesterol [7]. The chemical structures of these lipids are presented in Figure 1.2.

1.0.2 Physical Properties of Lipid Bilayers

The variety of chemical compositions, conditions, and environment can result in lipid bilayers that have a wide range of structures and dynamics. These are characterised

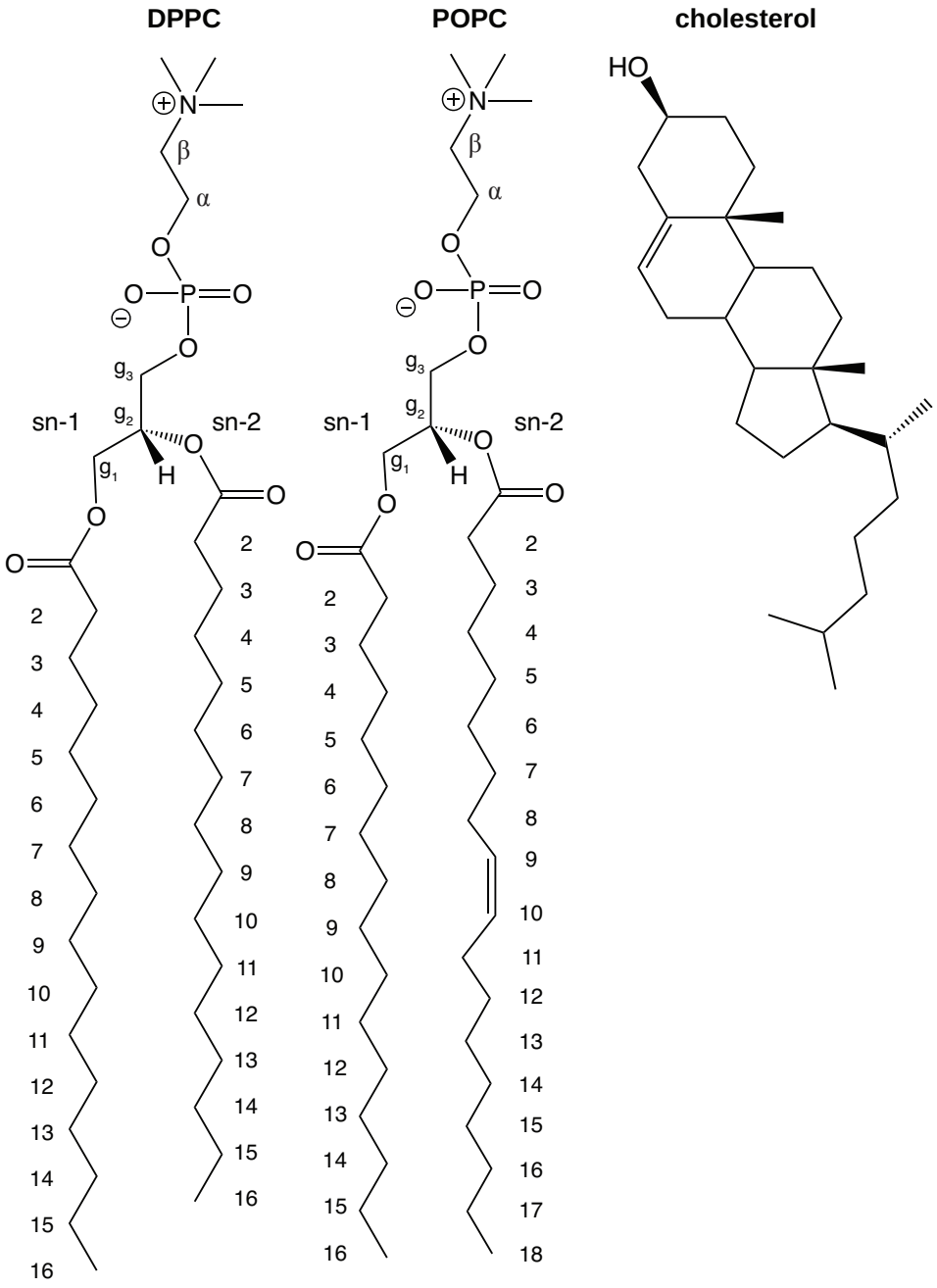

Figure 1.2: Chemical structures of DPPC and POPC lipids, as well as cholesterol.

by a set of physical properties. The thickness of the membrane can be described by the average distance between head groups or the average thickness of the acyl layer. In biological membranes, the headgroup–headgroup distance is typically about 40 Å [8]. The lipid headgroup area indicates the average surface area per lipid (A_L) of a bilayer. The headgroup area of a given lipid depends on the interactions between head groups, the hydration of the headgroups, and the packing and cohesion of the hydrocarbon tails [9]. Beyond the general structural parameters of thickness and headgroup area, NMR orientational order parameters, electron density profiles, compressibility, and other properties can also be used to describe the structure and dynamics of lipid bilayers [10]. The prediction of these properties is one way to test the validity of a model for a lipid bilayer [11].

1.1 Membrane Permeability

Cellular processes, like metabolism and signaling, require the passage of solutes across the membrane. Specialized membrane proteins selectively facilitate the passage of specific compounds, including ions [12] and sugars [13]. Other compounds can permeate directly through the lipid bilayer [14]. The rate at which a compound can pass through a bilayer can be described by the flux (J), which is the product of the concentration gradient (ΔC) across the bilayer and the permeability coefficient, P_m (Eqn. 1.1) [15].

$$J = -P_m \cdot \Delta C \tag{1.1}$$

The permeability coefficient depends on the composition of the membrane, the state of the system (e.g., temperature, T), and the properties of the molecule permeating. Models for understanding why bilayers are more permeable to some molecules

than others go back to the Meyer–Overton rule, which was developed from the observation that more hydrophobic molecules permeate membranes faster [16, 17]. This rule can be justified through a simple phase partitioning argument; to permeate a membrane, a solute must be removed from the aqueous solution and partition into the hydrophobic membrane interior. This partitioning will occur more readily for hydrophobic compounds.

Quantitative calculations of membrane permeability are possible using the inhomogeneous solubility–diffusion model, which defines P_m in terms of the Gibbs energy profile ($\Delta G(z)$) and the diffusivity ($D(z)$) of the permeating solute as a function of its position, z, along the transmembrane axis, and L is the thickness of the bilayer [18, 19, 20, 21]:

$$\frac{1}{P_m} = \int_{-L/2}^{L/2} \frac{e^{\Delta G(z)/RT}}{D(z)} \mathrm{d}z \tag{1.2}$$

Here, R is the gas constant and T is the temperature. The Gibbs energy and diffusivity profiles can be calculated using molecular simulations or estimated based on experimental data [22, 23]. In this model, the rate at which solutes permeate the membrane depends exponentially on the degree to which the solute can partition inside the membrane (i.e., the ΔG term) and depends linearly on its rate of diffusion inside the membrane, although both these terms can vary as a function of the bilayer depth (z).

The rate of permeation of small molecules such as H_2S across cell membranes is an important parameter in drug design and toxicology [24]. The solubility–diffusion model provides a means to calculate the membrane permeability coefficient of solutes using molecular simulations.

1.2 Permeation of Gases

Gas molecules play an important role in biochemistry. The most prominent examples are the gases O_2 and CO_2, which are involved in respiration. More recently, other gases have been found as serving biological roles. CO, NO, and H_2S have all been found to have endogenous biochemical roles as signaling molecules [25]. They are most significant as signalling molecules, so they have been termed "gasotransmitters." Although these gasotransmitters are highly toxic and hazardous in higher concentrations, in trace amounts, they serve a range of functions, such as regulation of the cardiovascular and nervous systems [26].

To serve their biological roles, gases must cross the biological membranes. Experimental and computational studies have concluded that O_2 and CO_2 can permeate cell membranes readily [27, 28, 29, 30, 31]. This is consistent with the solubility–diffusion model for membrane permeability because these non-polar molecules have a low solubility in water, so they tend to partition into the interior of the lipid bilayer [20]. The permeability of gasotransmitters is more controversial. Some researchers have concluded that gasotransmitters NO and H_2S can permeate cell membranes passively [22, 32, 33], while others have proposed that they pass through membrane-protein facilitators [34]. The permeability of CO has received less attention, although a computational study by Sugii et al. [35] concluded that it permeates membranes readily. A rigorous computational study would help resolve this debate.

1.2.1 Computer Simulation of Lipid Bilayers

The inherent disorder of lipid bilayers makes it necessary to describe the dynamics of these systems in order to capture the full complexity of their structure and dynamics. Molecular Dynamics (MD) simulations have been a very effective method for modeling

lipid-containing systems [36]. MD is used to simulate the motions of lipid, solvent, and other components of the system. These simulations are used to calculate the physical and transport properties of the system.

MD simulations rely on an integration algorithm that predicts the positions of the atoms at a small increment of time in the future (time step, δt) given the past motions of the system. The velocity Verlet algorithm is one popular MD algorithm [37]. The Verlet equation approximates the position of particles one time step in future from present time by using a Taylor series approximation [38]. This method predicts the positions of the atoms of the system at time $t + \delta t$ based on the current positions ($\mathbf{r}$), velocities ($\mathbf{v}$), forces on the atoms ($\mathbf{F}$), and the atomic masses (m). The equations to calculate the successive timesteps using the velocity Verlet algorithm are given in Eqns. 1.3 and 1.4.

$$\mathbf{r}(t + \delta t) = \mathbf{r}(t) + \mathbf{v}(t)\,\delta t + \frac{1}{2m}\mathbf{F}(t)\delta t^2, \tag{1.3}$$

$$\mathbf{v}(t + \delta t) = \mathbf{v}(t) + \frac{\mathbf{F}(t) + \mathbf{F}(t + \delta t)}{2m}\delta t. \tag{1.4}$$

This type of finite-step integration of the equations of motion is inherently approximate and the magnitude of the error has a quartic dependence on the length of the time step (i.e, $\mathcal{O}(\delta t^4)$). To limit this source of error, the time step for simulations of molecular systems must be small ($\delta t \approx 1 - 2$ fs) [39].

Standard Verlet integration of the equations of motion will sample the Microcanonical ensemble (NVE). For situations where it is necessary to sample the Isothermal-isobaric (NpT) or an Isothermal-isochoric (NVT) ensemble, the integration must be modified. To sample the canonical ensemble at a given temperature, T, the dynamics are coupled to a thermostat. For example, a Langevin thermostat is often used in

MD simulations of biomolecules [40]. Simulations of an isothermal-isobaric ensemble couple the equations of motion for the MD to both a thermostat and a barostat [41, 42].

To start a simulation, the atoms are assigned random velocities drawn from a Maxwell–Boltzmann distribution for the chosen temperature [43]. The MD algorithm is then iterated until a sufficient period has been calculated to provide sufficient sampling of the configurations available to the atoms of the system.

1.3 Force Fields

In order to perform an MD simulation, there must be a way to calculate the potential energy ($\mathcal{V}$) and forces on the atoms comprising the system for a given configuration of atoms. For large biomolecular systems, this is typically achieved by using molecular mechanical models. These models provide a simple, computationally-efficient description of the system. Atoms are typically represented as single point masses with partial atoms charges (q) assigned to represent the distribution of charge inside the molecules.

A force field is a mathematical description that is used to model how atoms and molecules interact with each other at the atomic and molecular level. The mathematical form of the force field is developed to capture the essential intra and intermolecular interactions that describe the relative potential energy of the possible conformations and intermolecular arrangements of molecules in the condensed phase.

The potential energy terms in a force field consist of both bonded ($\mathcal{V}_{bonded}$) and non-bonded ($\mathcal{V}_{non-bonded}$) terms [44]:

$$\mathcal{V}_{total} = \mathcal{V}_{bonded} + \mathcal{V}_{non-bonded}. \tag{1.5}$$

The bonded term describes interactions of atoms that are linked by covalent bonds.

Bond stretches ($\mathcal{V}_{bond}$) and bond-angle bending ($\mathcal{V}_{angle}$) are typically represented as simple harmonic oscillators. Rotations around dihedral angles ($\mathcal{V}_{dihedral}$) are represented using a sum of periodic functions:

$$\mathcal{V}_{bonded} = \sum_{ij}^{bonds} k_{b,ij}(r_{ij} - r_{eq,ij})^2 + \sum_{ijk}^{angles} k_{\theta,ijk}(\theta_{ijk} - \theta_{eq,ijk})^2 + \sum_{ijkl}^{dihedrals} \sum_{m} k_{\phi,ijkl,m} \cos\left(n_m(\phi - \tau_m)\right), \tag{1.6}$$

where $r_{eq,ij}$ is the equilibrium bond length, $\theta_{eq,ijk}$ is the equilibrium angle, $k_{b,ij}$ and $k_{\theta,ij}$ are the force constants, n_m is the number of periods in the potential for the complete rotation of this angle (i.e., its multiplicity), ϕ_{ijkl} is the torsional angle, and τ_m is the phase angle for torsional parameters.

The non-bonded component of the potential energy,

$$\mathcal{V}_{non-bonded} = \sum_{ij}^{pairs} \left[4\epsilon \left(\left(\frac{\sigma}{r_{ij}} \right)^{12} - \left(\frac{\sigma}{r_{ij}} \right)^{6} \right) + \frac{1}{4\pi\varepsilon} \frac{q_i q_j}{r_{ij}} \right], \tag{1.7}$$

consists of two components. The first is the 12-6 Lennard-Jones potential [45], which is intended to capture the repulsive and van der Waals interactions between atoms. The second term is Coulomb's law, which is intended to represent electrostatic interactions between partial atomic charges (q).

Here σ and ϵ are the Lennard-Jones well depths and radii for a given pair of atoms respectively, q_i is the partial charge of atom i, and ε is the vacuum permittivity constant. The equations used to describe the forces on the atom are collectively referred to as the force field [46].

1.4 Force Field Parameterization

Although most popular force fields calculate the potential energy of the system using an expression like Eqn 1.7, there are many definitions of the parameters required by this equation. A force field defines parameters for each atom type, chemical bond, dihedral angle, etc. Accurate parameters are very important in MD simulations because parameters that do not provide realistic predictions of the potential energy of the system will sample an incorrect distribution of conformational states.

Several molecular mechanical parameter sets for lipids have been developed, including the GROningen MOlecular Simulation (GROMOS) [47], Slipids [48], and Chemistry at HARvard Macromolecular Mechanics (CHARMM36) [49] parameters. Several studies have evaluated the ability of these models to predict the physical properties of lipid bilayers in order to validate these models. The CHARMM36 lipid force field has performed well on assessments of lipid headgroup areas, orientational order parameters, scattering data, etc.[11]

Simulations of water–lipid systems also require the selection of a molecular mechanical model for water. The solvation of the lipid head group has a significant effect on the properties of the lipid bilayer. The solubility difference that determines the rate of permeation is dependent on the solvation energy of the permeating solute. As a result, an accurate and robust model for water is essential for quantitative calculations of lipid systems. The CHARMM36 lipid model was developed for use with the CHARMM-modified variant of the Transferable Intermolecular Potential with 3 Points (TIP3P) water model. This modified model is denoted in this thesis as mTIP3P. The original TIP3P model was developed by Jorgensen et al. in 1983 [50]. This model has an anomalously high dielectric constant and self-diffusion coefficient, which limits its accuracy in the calculation of quantities like permeability coefficients

[51, 52]. TIP4P-FB and TIP3P-FB are two water models that are optimized using the ForceBalance (FB) software [53]. These reparameterized water models are more accurate in terms of the dielectric constant and transport properties, which could allow for more accurate simulations of systems containing water and lipids, although these models have not been validated for use with the CHARMM36 lipid force field.

1.5 Calculation of Gibbs Energies

The relative Gibbs energies of configurational states are not immediately available from a conventional MD simulation. Instead, Gibbs energies are often calculated using specialized simulation algorithms. The methods used in this thesis are briefly summarized here.

1.5.1 Umbrella Sampling

Calculation of membrane permeability using the solubility–diffusion model requires the Gibbs energy profile of the translocation of the solute along the transmembrane axis (z). Conventional MD simulations sample the Boltzmann distribution of states, where the probability (P) that the solute will be located at position $\mathbf{r}$ is exponentially dependent on the potential energy ($\mathcal{V}$) of that configuration:

$$P(\mathbf{r}) \propto \exp\left(\frac{-\mathcal{V}(\mathbf{r})}{RT}\right). \tag{1.8}$$

As the probability a state is sampled decreases exponentially with its potential energy, higher energy configurations will only be sampled rarely. As a consequence, higher energy portions of the Gibbs energy profile, such as the reaction barriers, may not be sampled sufficiently in a conventional MD simulation.

Umbrella sampling is a simulation method that allows complete Gibbs energy

profiles to be calculated efficiently [54, 55]. These calculations use the combined data of multiple equilibrium MD simulations where the solute is restrained to different positions along the z coordinate. Commonly, harmonic restraints are employed, where k_{rest} is the spring constant and the reference position of the restraint is $z_{0,i}$ so that

$$\mathcal{V}_{umb,i}(\mathbf{r}) = \frac{1}{2} k_{rest} \left(z - z_{0,i}\right)^2 . \tag{1.9}$$

Simulations using this biased potential will yield a biased probability distribution,

$$P_{biased,i}(\mathbf{r}) \propto \exp\left(\frac{-\left[\mathcal{V}(\mathbf{r}) + \mathcal{V}_{umb,i}(\mathbf{r})\right]}{RT}\right). \tag{1.10}$$

The unbiased probability distribution can be deduced from this biased probability distribution by using the rules of exponents to separate the exponential distribution in Eqn. 1.10:

$$P_{biased,i}(\mathbf{r}) \propto \exp\left(\frac{-\mathcal{V}(\mathbf{r})}{RT}\right) \cdot \exp\left(\frac{-\mathcal{V}_{umb,i}(\mathbf{r})}{RT}\right). \tag{1.11}$$

The first exponential factor on the the right hand side of this equation is the unbiased probability distribution, so the biased probability distribution can be related to the unbiased distribution,

$$P_{biased,i}(\mathbf{r}) \propto P_{unbiased,i}(\mathbf{r}) \cdot \exp\left(\frac{-\mathcal{V}_{umb,i}(\mathbf{r})}{RT}\right). \tag{1.12}$$

A range of methods can be used to combine these probability distributions into a single Gibbs energy profile. In this thesis, the Weighted Histogram Analysis Method (WHAM) is used [56]. This method generates histograms describing the biased probability distributions into discrete bins along the profile. WHAM calculates the relative Gibbs energy offset of each of these distributions on the profile using an iterative, self-consistent algorithm, which provides an unbiased probability distribution of the

full profile ($P_{unbiased}$). The Gibbs energy of bin k (ΔG_k) can be calculated from this probability distribution using the relation,

$$\Delta G_k = -RT \ln P_{unbiased,k}. \tag{1.13}$$

1.5.2 Free Energy Methods

Umbrella sampling can be used to calculate the Gibbs energy profile along a coordinate, but the solvation of a solute requires a different approach. Molecular solvation energies are generally calculated by an "alchemical" decoupling scheme, where the Gibbs energy required to "turn off" the molecule–solvent intermolecular interactions is calculated. This is effected by defining two equations for the potential energy of two states, $\mathcal{V}_0$ and $\mathcal{V}_1$. A new potential, $\mathcal{V}_\lambda$, is defined as a linear combination of these two potentials where λ is a scalar coupling parameter that ranges between 0 and 1:

$$\mathcal{V}_\lambda = (1-\lambda)\mathcal{V}_0(\mathbf{r}) + \lambda\mathcal{V}_1(\mathbf{r}). \tag{1.14}$$

In this context, $\mathcal{V}_0$ is the potential energy of the system for a state where a mode of interaction is at its normal strength (e.g., electrostatic, dispersion...) and $\mathcal{V}_1$ is the potential energy of the system when the strength of the interaction is zero.

The relative Gibbs energies of these states can be calculated by the process of thermodynamic integration [57], where the derivative of $\mathcal{V}_\lambda$ is integrated with respect to the coupling parameter λ:

$$\Delta G_{\lambda=0\rightarrow\lambda=1} = \int_{\lambda=0}^{\lambda=1} \left\langle \frac{\partial \mathcal{V}_\lambda}{\partial \lambda} \right\rangle_\lambda \mathrm{d}\lambda. \tag{1.15}$$

Alternatively, the relative Gibbs energies of the two states can be calculated using the free energy perturbation (FEP) technique [58]. In this method, an MD simulation

is performed using the potential energy function of the first state and the relative Gibbs energy is calculated from an ensemble average of the Boltzmann-weighted difference of the potential energy in the two states:

$$\Delta G_{\lambda=0\rightarrow\lambda=1} = -RT \ln \left\langle \exp\left(\frac{-[\mathcal{V}_{\lambda=1} - \mathcal{V}_{\lambda=0}]}{RT}\right)\right\rangle_0 . \tag{1.16}$$

These methods can be used to calculate the solvation energy of a solute by defining two states of the system. In first state, the solute interacts with the solvent through the standard intermolecular interactions. In the second state, these interactions are entirely absent. This procedure can be divided into stages where the electrostatic, dispersion, and repulsive components of the solvation energy are calculated in successive steps. The sum of the Gibbs energies of each component yields the total solvation energy:

$$\Delta G = \Delta G_{elec.} + \Delta G_{disp.} + \Delta G_{repul.}. \tag{1.17}$$

The electrostatic component can be performed through a straightforward TI calculation where the solute charges are their standard values in the beginning state but are set to zero in the final state.

Calculation of the dispersion and repulsive components is more complex because conventional force fields combine these force into the Lennard-Jones potential. One popular route is the Weeks–Chandler–Andersen decomposition [59]. In this decomposition, the original Lennard-Jones potential is recast as the sum of repulsive and dispersion components:

$$\mathcal{V}_{LJ}(r) = \mathcal{V}_{rep.}(r) + \mathcal{V}_{disp.}(r). \tag{1.18}$$

The dispersion interaction is defined by the shifted potential:

$$\mathcal{V}_{disp.}(r) = \begin{cases} -\varepsilon_{ij}, & r \leq R^*_{ij} \\ \varepsilon_{ij}\left[\left(\frac{R^*_{ij}}{r}\right)^{12} - 2\left(\frac{R^*_{ij}}{r}\right)^{6}\right], & r > R^*_{ij} \end{cases} \tag{1.19}$$

In this equation, R^*_{ij} is the average of the radii of the minima of the Lennard-Jones interaction of like pairs i and j (i.e., $R^*_{ij} = (R^*_{ii} + R^*_{jj})/2$). The Gibbs solvation energy corresponding to this interaction can also be calculated by a standard TI calculation where the magnitude of dispersion term is scaled to zero, leaving only the repulsive potential.

The solvent–solute repulsive interactions require special attention. These interactions cannot be continuously scaled to zero because the polynomial form of the Lennard-Jones $1/r^{12}$ repulsive term becomes infinite as $r \to 0$. Instead, free energy perturbation (FEP) techniques can be used, where the Gibbs energy of decoupling the repulsive component of the solute from the solvent is calculated by calculating the sum of the Gibbs energies to increase a scaling parameter, s, from 0 (non-interacting) to 1 (fully-interacting). The potential energy for pairwise interactions is rewritten to depend on s such that it decreases to zero continuously as $s \to 0$ (Eqn. 1.20).

$$\mathcal{V}_{rep}(r;s) = \begin{cases} \varepsilon_{ij}\left\{\frac{(R^*_{ij})^{12}}{\left[r^2+(1-s)^2(R^*_{ij})^2\right]^6} - \frac{(R^*_{ij})^{6}}{\left[r^2+(1-s)^2(R^*_{ij})^2\right]^3} + 1\right\}, & r \leq R^*_{ij}\sqrt{1-(s-1)^2} \\ 0, & r > R^*_{ij}\sqrt{1-(s-1)^2} \end{cases} \tag{1.20}$$

Deng and Roux [60] found that 9 stages were sufficient to sample the repulsive component of the Gibbs energy of solvation ($s = 0.0 \to 0.2, 0.2 \to 0.3, 0.3 \to 0.4, 0.4 \to 0.5, 0.5 \to 0.6, 0.6 \to 0.7, 0.7 \to 0.8, 0.8 \to 0.9$, and $0.9 \to 1.0$). Using these methods, solvation energies of molecules in liquids can be calculated rigorously.

A limitation of these methods is that the MD simulations may be inefficient in sampling the configuration space because of large changes in the hydration structure that may accompany the decoupling of the solute from the solvent. This can be addressed in part using replica exchange MD. In this method, the simulations of all Thermodynamic Integration / Free Energy Perturbation (TI/FEP) windows and stages are performed simultaneously on different computing processors. Periodic attempts are made to exchange the configurations of neighboring "replicas", which are typically those with the most similar λ and s values. The potential energy change that results from the exchange replicas i and j is calculated ($\Delta\mathcal{V} = \mathcal{V}_j(\mathbf{r}_i) - \mathcal{V}_i(\mathbf{r}_j)$) and used to calculate the acceptance probability of the exchange based on the Metropolis criterion [61]:

$$P_{acc}(i \leftrightarrow j) = \begin{cases} 1, & \Delta\mathcal{V} < 0 \\ \exp\left(\frac{-\Delta\mathcal{V}}{RT}\right), & \Delta\mathcal{V} \geq 0 \end{cases} \tag{1.21}$$

The theory and methods of replica exchange MD is described in Refs. [62] and [63].

1.6 Thesis Outline

An accurate, atomic-scale model would make it possible to better understand the interactions between gasotransmitters and cell membranes. In this thesis, molecular simulation methods are validated and then applied to model the membrane permeation of the gasotransmitters. In Chapter 2 the evaluation of the CHARMM36 lipid model with the TIP3P-FB and TIP4P-FB water models is presented. These water models would resolve issues in membrane permeation simulations that stem from the high dielectric constant and low viscosity that is present when the standard TIP3P

water model is used. In Chapter 3, we make use of the water model validated in Chapter 2 to perform more accurate calculations of the permeation of gasotransmitters through model membranes. The effect of the cholesterol content of lipid bilayers on the permeation of these compounds is also explored.

Chapter 2

Simulations of Lipid Bilayers Using the CHARMM36 Lipid Model and the TIP3P-FB and TIP4P-FB Water Models

Some of the content of the chapter has been published in the journal *PeerJ*:
Sajadi, F., Rowley, C. N., Simulations of lipid bilayers using the CHARMM36 force field with the TIP3P-FB and TIP4P-FB water models, *PeerJ*, **2018**, e5472, DOI: 10.7717/peerj.5472

2.1 Abstract

The CHARMM36 force field for lipids is widely used in simulations of lipid bilayers. The CHARMM family of force fields was developed for use with the mTIP3P water model. This water model has an anomalously high dielectric constant and low

viscosity, which limits its accuracy in the calculation of quantities like permeability coefficients. The TIP3P-FB and TIP4P-FB water models are more accurate in terms of the dielectric constant and transport properties, which could allow more accurate simulations of systems containing water and lipids. To test whether the CHARMM36 lipid force field is compatible with the TIP3P-FB and TIP4P-FB water models, we have performed simulations of DPPC and POPC bilayers. The calculated lipid headgroup area, compressibility, orientational order parameters, and X-ray form factors are in good agreement with the experimental values, indicating that these improved water models can be used with the CHARMM36 lipid force field without modification when calculating membrane physical properties. The water permeability predicted by these models is significantly different; the mTIP3P-model diffusion in solution and at the lipid–water interface is anomalously fast due to the spuriously low viscosity of mTIP3P-model water, but the Gibbs energy profile of permeation is higher for the TIP3P-FB and TIP4P-FB models due to their high excess chemical potentials.

2.2 Introduction

Realistic molecular dynamics (MD) simulations of lipid-containing systems like bilayers, vesicles, and membrane–protein systems require accurate molecular mechanical force fields for lipids. A variety of lipid models have been developed, including the Berger [64], Slipids [48], and the CHARMM models [49]. These models have been carefully parametrized using *ab initio* data and the empirical properties of bilayers. The performance of these models is evaluated based on their ability to predict empirical data regarding the structure and dynamics of lipid properties.

A common practice in evaluating force fields has been to evaluate the ability of these models to predict physical descriptors of lipid bilayers. The headgroup area (A_L)

corresponds to the average surface area occupied by one lipid in the bilayer. The area compressibility (K_A) of the bilayer indicates the energetic cost of an elastic expansion of the bilayer surface area. Poger et al. [10] noted that these properties are inferred from several different experimental techniques, so the range of reported experimental values can be broad, including for lipids that are commonly used in simulations.

Scattering experiments have provided more direct data to validate the ability of force fields to predict the structure of bilayers [65, 66, 67, 68, 69, 70]. Form factors from X-ray scattering experiments can be used to infer the transmembrane electron density distribution ($\rho(z)$), which is particularly sensitive to the position of phosphates of the lipid headgroups. Neutron scattering can be used to calculate Neutron Scattering Length Density (NSLD) profiles as a function of bilayer depth. The NSLD profiles from neutron scattering experiments were performed with D_2O because there is a sharp difference between the scattering lengths of the aqueous deuterons and the lipid protons, providing a measure of the hydrophobic thickness of the bilayer. The X-ray and neutron scattering profiles calculated from MD simulations can be compared to the profiles inferred from these experiments. The experimental and calculated form factors can be compared directly [69].

Orientational order parameters are another method for validating lipid models [71]. The orientational order parameters (S_{CH}) of the head groups and acyl chains of the lipid tails provide a measure of the configurational flexibility of the lipids tails as a function of position along the lipid chain. These parameters can be determined from the Nuclear Magnetic Resonance (NMR) coupling constants of lipids. This provides an experimental test of the predicted conformational flexibility of the lipids as a function of the bilayer depth.

The development of lipid models is ongoing because some properties of lipid bilayers have proven difficult to predict accurately using existing models. For example,

established non-polarizable force fields typically overestimate the membrane dipole potential (MDP, $\phi(z)$) of lipid bilayers [72]. MDP arises from changes in the electrostatic potential between the solution and the various components of the bilayer, and reflects the average strength of interaction of a test charge at different bilayer depths [73].

The CHARMM36 lipid model has proven to be quantitatively accurate for lipid bilayer properties such as thickness, headgroup area, orientational order parameters, and form factors [49]. Simulations of lipids require the selection of a model for the water molecules in the system. The CHARMM36 lipid model was parameterized for use with the mTIP3P water model. This water model underestimates the viscosity of liquid water [51], resulting in spuriously high rates of self-diffusion. This model also overestimates the dielectric constant of water [52], so the physical description of the partitioning of charged or polar solutes between the aqueous solution and the bilayer interior is imperfect. These issues are sources of error in quantitative calculations of some membrane processes, particularly for transport properties like the rate of permeation of water and other solutes across a bilayer [23, 74, 75].

Table 2.1: Physical properties of water predicted by the mTIP3P, TIP3P-FB, and TIP4P-FB water models (298.15 K, 101.325 kPa). TIP3P-FB and TIP4P-FB values are reproduced from Ref. [53].

property	expt.	mTIP3P	TIP3P-FB	TIP4P-FB
density (ρ) / g cm^{-3}	0.997	0.98	0.995	0.996
enthalpy of vaporization (ΔH_{vap}) / kcal mol^{-1}	10.52	9.81	10.71	10.80
dielectric constant (ϵ)	78.5	104	81.3	77.3
diffusivity (D) / 10^{-5} cm^2 s^{-1}	2.29	6.48	2.28	2.21

The predicted properties of liquid water vary significantly with how the molecular mechanical model represents the structure and intermolecular interactions of water molecules [76, 77]. The TIP3P model was developed in 1983 by Jorgensen et al. [50].

This model features partial atomic charges centered on the hydrogen and oxygen atoms and holds a rigid geometry that is consistent with water in the liquid phase ($\angle$HOH = 104.5°, r_{OH} = 0.9572 Å). In the original TIP3P model, there is a single Lennard-Jones interaction potential between oxygen atoms, but there is a popular variant where there are also Lennard-Jones sites on the hydrogen atoms. This model is referred to as the mTIP3P or CHARMM TIP3P model. The structures and parameters of these models are presented in Figure 2.1. The mTIP3P model has been used in the development of the CHARMM force fields, so this model has been prescribed for use in simulations using these force fields. To be consistent with this practice, in this chapter, the properties of the standard CHARMM36 bilayer models are accessed using the mTIP3P water model rather than the TIP3P model.

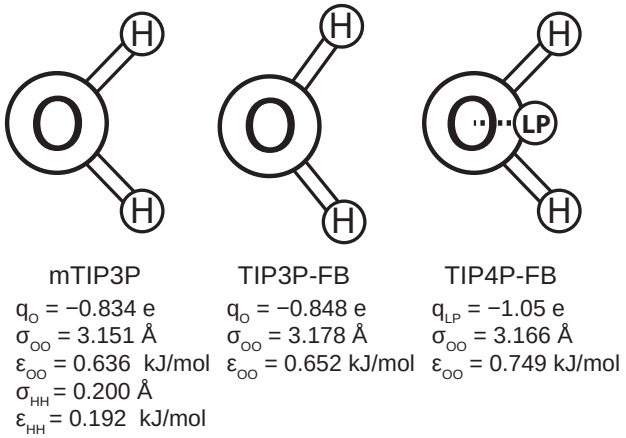

Figure 2.1: Schematics of the mTIP3P, TIP3P-FB, and TIP4P-FB water models. The electrostatic and Lennard-Jones parameters are listed beneath each model.

The TIP3P/mTIP3P models predate computational algorithms such as Particle Mesh Ewald (PME) electrostatics, so these parameters are not optimal for use with modern simulation methods. Although this simple model performs reasonably well

for predicting the density and enthalpy of vaporization of water under ambient conditions, its dielectric constant and diffusivity coefficients are anomalously high (Table 2.1). Many alternative water models have been developed that describe the physical properties of water more realistically. In the TIP4P model, a 4th charge site is added along the HOH bisector. The original TIP4P model has been reparameterized several times, including the development of the TIP4P-Ew and TIP4P/2005 models [78]. These models describe many of the physical properties of water with remarkable accuracy, although the dielectric constants were systematically lower than the experimental values ($\epsilon \approx 60$) [53]. More complex models with additional charge sites have been defined (e.g., TIP5P), although they have not become widely adopted in molecular dynamics simulations.

Despite the existence of models that describe the properties of water more accurately, TIP3P and mTIP3P have remained the mainstay in biomolecular simulation. This is because established force fields like CHARMM36 have not been comprehensively validated for use with other water models and bilayer properties can be sensitive to the water model used. Piggot et al. [11] found that DPPC lipid bilayers underwent a phase transition to a tilted gel phase when simulated with the CHARMM36 force field, the TIP3P water model, and energy-based non-bonded switching functions instead of the CHARMM-type force-based non-bonded switching functions with mTIP3P water. This occurred in a simulation performed at 50 °C, where DPPC lipid bilayers are experimentally known to exist in a fluid phase. This indicates that these simulations resulted in an incorrectly high stability for the tilted gel phase relative to the fluid phase. Recently, Javanainen et al. [79] showed that the CHARMM36 lipid force field predicted the properties of POPC and DPPC monolayers accurately when used with the four-point Optimal Point Charge (OPC) model, suggesting that it may be possible to use the existing CHARMM36 lipid model with more accurate water

models. The OPC water model is described in Ref. [80].

Recently, Wang et al. developed the ForceBalance (FB) code, which allows the parameters of a molecular mechanical model to be optimized systematically [53]. This code was used to develop the TIP3P-FB and TIP4P-FB water models, which were parameterized to reproduce the enthalpy of vaporization, density, dielectric constant, isothermal compressibility, heat capacity, and thermal expansion coefficient of liquid water. Like the mTIP3P model, the TIP3P-FB model has partial atomic charges on each of the nuclear centers, but the ∠HOH angle is increased from 103.5° to 108.1° and the O–H bond length is increased to 1.01 Å. The TIP4P-FB model holds the same molecular geometry as TIP3P, but the charge on the oxygen atom is shifted to a virtual site located on the bisector of the ∠HOH (Figure 2.1). For all three models, there is a non-bonded interaction site that is centered at the oxygen atom. The potential energy of this interaction ($\mathcal{V}_{LJ}(r)$) is calculated using the Lennard-Jones equation,

$$\mathcal{V}_{LJ}(r) = 4\varepsilon_{OO}\left[\left(\frac{\sigma_{OO}}{r}\right)^{12} - \left(\frac{\sigma_{OO}}{r}\right)^{6}\right] \tag{2.1}$$

where ε_{OO} and σ_{OO} are the well-depth and atomic radius parameters and r is the distance between the oxygen atoms. The mTIP3P model also has weakly-interacting Lennard-Jones potentials for atomic pairs involving the hydrogen atoms.

TIP3P-FB and TIP4P-FB water models accurately describe many of the physical properties of water, including viscosity and dielectric constant. Further, the TIP4P-FB model predicts the variation of these properties with temperature more accurately but does not underestimate the dielectric constant ($\varepsilon = 78$) like other 4-point water models. Using the same procedure, the ForceBalance method can be used to develop force field parameters for other components, providing a systematic route to develop improved force fields that are based on the FB water models. Lipid simulations using

improved water models, like TIP3P-FB or TIP4P-FB, could provide more accurate descriptions of phenomena like transport properties and partitioning, but it has not been shown that these models are compatible. Lipid bilayer properties are sensitive to effects like headgroup solvation, so changing the water model could cause the bilayer properties predicted by these simulations to be less accurate.

In this chapter, we report the physical and structural properties of lipid bilayers described using the CHARMM36 lipid model, in combination with the mTIP3P, TIP3P-FB, and TIP4P-FB water models. The lipid headgroup areas, electron density profiles, X-ray form factors, membrane dipole potential, and orientational order parameters were calculated from these simulations and used to model the lipid bilayers. DPPC, a saturated lipid, and POPC, an unsaturated lipid,il were used to test these models (Figure 1.2). These lipids were chosen because they are commonly used in simulation and experimental studies of model bilayers and there is extensive experimental data on their properties. We also calculate the Gibbs energy and diffusivity profiles of water molecules permeating across a POPC bilayer using these three water models to calculate the membrane permeability.

2.3 Computational Methods

2.3.1 Lipid Bilayer Simulations

Pure DPPC and POPC bilayers were constructed using the Membrane Builder feature of the CHARMM-GUI interface [81, 82, 83, 84, 85]. All simulations were performed using Nanoscale Molecular Dynamics (NAMD) 2.12 [86]. A 2 fs time step was used. Properties were calculated from the average of three simulations that were each 500 ns in length, following 100 ns equilibration simulations. Uncertainties of

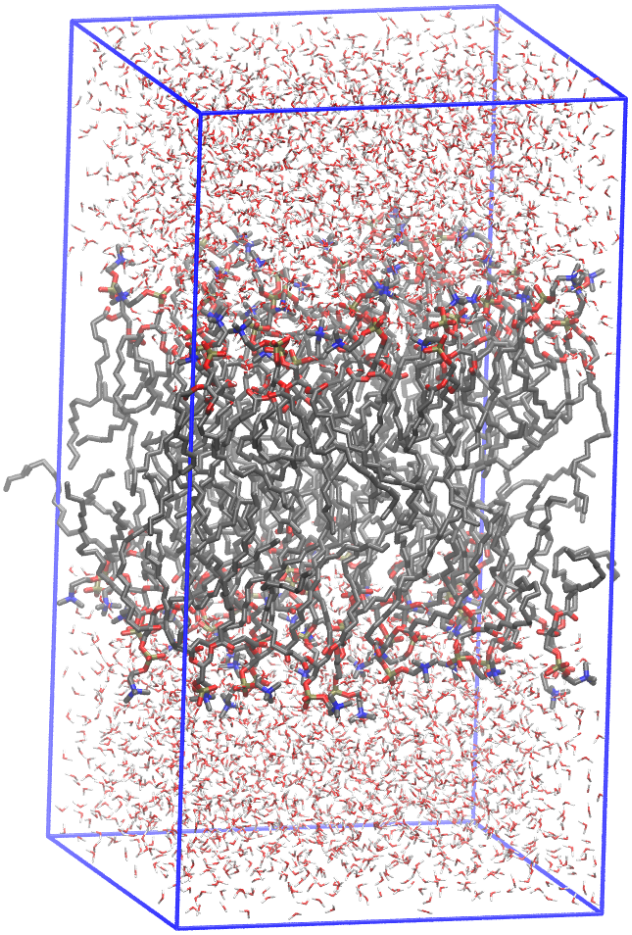

Figure 2.2: A rendering of the simulation cell used in the simulations of a POPC lipid bilayer.

the calculated properties were calculated from the standard deviation of the calculated properties of these three simulations. The DPPC simulation cell contained 74 lipids and 4241 water molecules, while the POPC simulation cell contained 68 lipids and 4253 water molecules. The approximate dimensions of the simulation cells were 44 Å×44 Å×110 Å. An example simulation cell is depicted in Figure 2.2. DPPC bilayers were simulated at 323 K, while the POPC bilayers were simulated at 303 K.

Lennard-Jones interactions were scaled to zero at a distance of 12 Å. CHARMM-style force-based switching was applied to the Lennard-Jones potential (i.e., the "vdwForceSwitching on" option in NAMD). The CHARMM36 lipid models were developed

using this switching function and simulations using different treatments of non-bonded interactions can result in significant differences in lipid bilayer properties [11]. Long-range electrostatic interactions were described using the Particle Mesh Ewald method [87] with a grid spacing of 1 Å. Bonds containing hydrogen atoms were kept rigid using the SHAKE algorithm [88]. The bilayers were simulated under NPT conditions (i.e., no applied surface tension) using a Langevin thermostat with a friction coefficient of 1 ps^{-1} and a Nosé–Hoover Langevin piston barostat with a decay period of 50 fs. The lipids were represented using the CHARMM36 parameters for DPPC and POPC, while the water molecules were represented using the mTIP3P [50, 89, 90], TIP3P-FB, and TIP4P-FB models [53]. Electron density and neutron scattering profiles were calculated using the Density Profile extension [91] of Visual Molecular Dynamics (VMD). These profiles were transformed into reciprocal space using the theory described by Benz et al. [92] and atomic parameters of the SimToExp code [69].

These simulations are performed under isothermal-isobaric conditions (NPT) where the X and Y lengths of the simulation cell are constrained to be equal. This allows the simulation to sample the distribution of bilayer surface areas. From this distribution, the average headgroup area (A_L) was calculated from the average of the X-Y area (calculated from the X and Y lengths of the orthorhombic simulation cell: L_X and L_Y) and the number of lipids per leaflet (n_L),

$$A_L = \frac{\langle L_x L_y \rangle}{n_L}. \tag{2.2}$$

The compressibility (K_A) was calculated from the fluctuation of the headgroup area in an equilibrium simulation,

$$K_A = \frac{k_B T \langle A_L \rangle}{n_L \langle \delta A_L^2 \rangle}. \tag{2.3}$$

2.3.2 Orientational Order Parameters

The orientational order parameters (S_{CH}) were calculated using the MEMPLUGIN [93] extension of VMD 1.9.2 [94] and the calcOrderParameters script of the NMRlipids project [95]. The orientational order parameters are calculated from the angle (θ) formed between the designated C–H bond and a vector normal to the surface of the bilayer using the relation,

$$S_{CH} = \left| \left\langle \frac{3\cos^2(\theta) - 1}{2} \right\rangle \right| \tag{2.4}$$

2.3.3 Membrane Dipole Potential

The MDP was calculated from the charge density along the transmembrane axis of the simulation cell ($\zeta(z)$) averaged over the length of the simulations. The MDP was calculated numerically from these data using the relation [96]:

$$\phi(z) - \phi(0) = -\frac{1}{\varepsilon_0} \int_{z_0}^{z} \int_{z_0}^{z'} \zeta(z'')\mathrm{d}z''\mathrm{d}z'. \tag{2.5}$$

The charge density was calculated from an average of the partial atomic charges centered at the nuclei.

2.3.4 Permeability

The solubility–diffusion model was used to calculate the water permeability of the POPC bilayer (Eqn. 1.2). The Gibbs energy profile was calculated using an umbrella sampling simulation, where the position of one water molecule was restrained to a designated position with respect to the center of mass of the bilayer along the z-axis. A harmonic restraint with a spring constant of 2.5 kcal/mol/Å^2 was used to restrain the solute. The initial windows were generated by placing the permeating water molecule

at the designated position along the z-axis and a random position on the X-Y plane. The bilayer structure for each window was selected from a random frame from the long-timescale bilayer simulations. A 120 ns molecular dynamics simulation was performed for each window, where the first 20 ns was discarded as equilibration. Although the calculation of the Gibbs energy profile of permeation for charged solutes like arginine requires extremely long simulations (e.g., μs) [97], the Gibbs energy profile for permeation of small neutral solutes can be calculated from these comparatively short simulations [98]. The Gibbs energy profile was calculated from these windows using the Weighted Histogram Analysis Method (WHAM) [55, 56, 99]. The diffusivity profile was calculated from the average of three 2 ns NVE simulations where the solute was restrained using a 20 kcal/mol/Å^2 harmonic force constant. The diffusivity was calculated from these time series using generalized Langevin analysis of the position autocorrelation function of these time series [100, 101].

2.3.5 Calculation of Transfer Energies

The transfer energies and excess chemical potentials were calculated using the staged thermodynamic-integration/free-energy-perturbation (TI/FEP) technique of Deng and Roux [60] that was described in Chapter 1.5.2. The electrostatic component was calculated by scaling the solute charges to zero through scaling factors of λ = [0.0, 0.1, 0.2, 0.3, 0.4, 0.5, 0.6, 0.7, 0.8, 0.9, 1.0]. The dispersion and repulsive components were calculated using a Weeks–Chandler–Andersen decomposition of the Lennard-Jones terms of the solute. The dispersion component was calculated by an 11-window thermodynamic integration calculation with λ = [0.0, 0.1, 0.2, 0.3, 0.4, 0.5, 0.6, 0.7, 0.8, 0.9, 1.0]. The repulsive component was calculated using a 9-stage free energy perturbation calculation. Each window/stage of the simulation was simulated for 1 ns for equilibration following by 2 ns of sampling. Replica exchange was used to allow

exchanges between neighboring windows of the TI/FEP simulation at 2 ps intervals, following the procedure described in Jiang et al. [63]. Gibbs energies were calculated using WHAM [56]. A complete description of these methods is provided in Chapter 1.5.2.

2.4 Results

2.4.1 Headgroup Area and Compressibility

The headgroup areas and compressibilities of the bilayer models calculated from the molecular dynamics simulations are presented in Tables 2.2 and 2.3, respectively. Although all three water models give headgroup areas within a 1.2 Å range, a Student's t-test shows the distributions are statistically distinct ($p < 0.0001$) for all pairs of distributions. The TIP3P-FB water model tends to predict smaller headgroup areas, which puts it into closer agreement with experiment than the mTIP3P model for the DPPC bilayer but worse agreement for the POPC bilayer. The mTIP3P and TIP4P-FB models give similar headgroup areas. The DPPC compressibilites predicted by the FB models are larger and in better agreement with the experimental value. The POPC compressibilities are less systematic, as the TIP4P-FB model predicts a lower compressibility than the mTIP3P model but the TIP3P-FB model predicts a higher compressibility.

2.4.2 C–H Orientational Order Parameters

The calculated acyl C–H orientational order parameters, and those determined experimentally, are plotted in Figure 2.3. The acyl C–H orientational order parameters are generally insensitive to the water model and simulations using any of the three

Table 2.2: Lipid headgroup areas for DPPC and POPC bilayers in $Å^2$. Experimental values are taken from Ref. [70]. The uncertainties of the calculated values are calculated from the standard deviation of the results from three independent simulations of the bilayer.

water model	DPPC	POPC
mTIP3P	61.1 ± 0.1	64.6 ± 0.6
TIP3P-FB	60.3 ± 0.7	64.0 ± 0.6
TIP4P-FB	61.5 ± 0.1	65.2 ± 0.4
expt.	63.1 ± 1.3	64.3 ± 1.3

Table 2.3: Compressibility for DPPC and POPC bilayers in dyne/cm. The uncertainties of the calculated values are calculated from the standard deviation of the results from three independent simulations of the bilayer.

water model	DPPC	POPC
mTIP3P	189.8 ± 8.00	237.2 ± 10.60
TIP3P-FB	265.8 ± 38.39	264.8 ± 9.99
TIP4P-FB	230.5 ± 10.40	214.6 ± 10.23
expt.	231 [a]	180–330 [b]

[a] Ref. [66], [b] Ref. [102]

models predict orientational order parameters that are in good agreement with the experimental values. This trend holds for the acyl groups in the upper region of the chain that are close to the water layer, which indicates that the lipid–water interface is similar for all three water models.

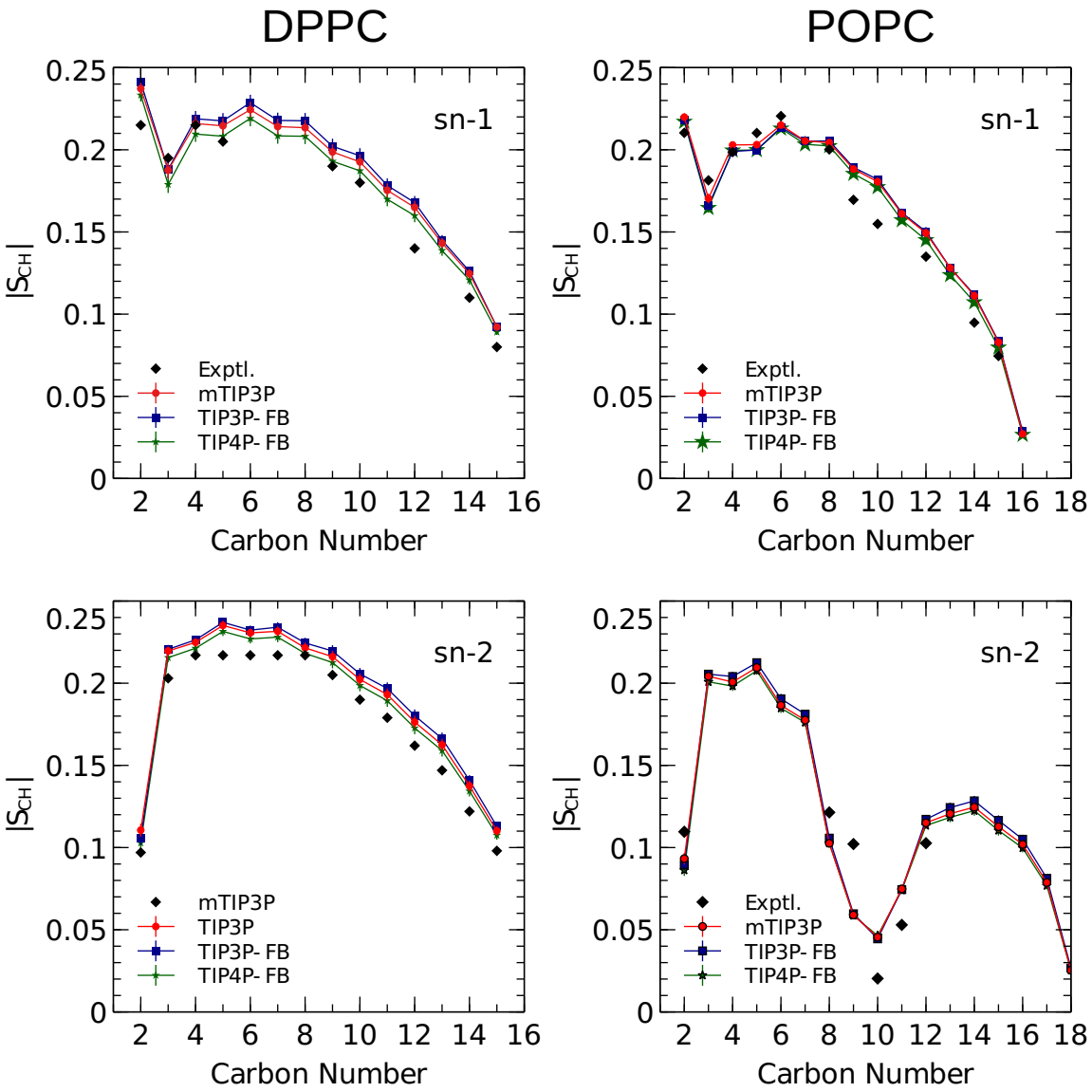

Figure 2.3: NMR deuterium orientational order parameters ($|S_{CD}|$) for the lipid tails of the DPPC and POPC bilayers calculated from simulations of the bilayers with the mTIP3P, TIP3P-FB, and TIP4P-FB water models. The upper plots show the profile for the first chains (sn-1), while the lower plots show the profiles for the second chain (sn-2). Experimental values are reproduced from Refs. [103, 104, 105, 106]. In most cases, the values from the simulations are so similar that the points lie on top of each other. The numbering of the positions on the acyl chains is illustrated in Figure 1.2.

The orientational order parameters of the atoms in the lipid headgroups are presented in Figure 2.4. These positions tend to show a lower degree of order than the acyl chains (i.e., $|S_{CH}| < 0.1$). All models are in reasonably good agreement with the experimental values. The results of the TIP3P and TIP3P-FB model simulations are in close agreement, while the TIP4P-FB model predicts incrementally more negative orientational order parameters for the POPC glycerol positions (i.e., g_1, g_2, and g_3).

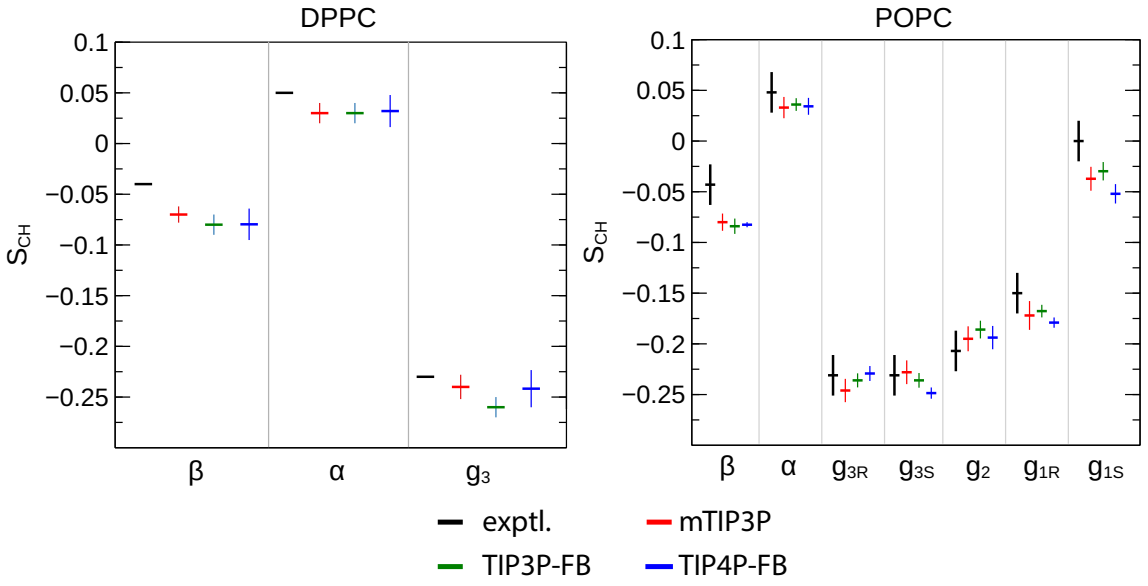

Figure 2.4: NMR orientational order parameters (S_{CH}) for the lipid headgroups of the DPPC (left) and POPC (right) bilayers calculated from simulations of the bilayers with the mTIP3P, TIP3P-FB, and TIP4P-FB water models. Experimental values for DPPC are taken from Ref. [107]. Experimental values for POPC are taken from Ref. [108]. The assignments of the orientational order parameters follow those presented in Ref. [95]. The labeling of the positions of the headgroup is illustrated in Figure 1.2.

The sn-2 chain of POPC contains a double bond at the C9 position. This unsaturated segment introduces a significant degree of disorder in the membrane due to the abrupt change in angle in the lipid tail that frustrates the orderly packing of the chain. The qualitative trend of the decrease in order in the sn-2 chain is captured by the CHARMM36 POPC lipid model using any of the three water models. This model

underestimates the orientational order parameter of the C9 position but overestimates orientational order parameter of the C10 position. The Berger lipid model performs somewhat better for these positions [108], so revision of the CHARMM36 parameters for unsaturated segments may improve the performance of this model for this type of lipids.

2.4.3 Bilayer Electron Density and Scattering

The calculated electron density profiles for the three water models are presented in Figure 2.5. The profiles are similar for all three water models, although for the DPPC bilayer, the electron density maximum is slightly higher and occurs at a higher value of Z for the TIP3P-FB model in comparison to the mTIP3P model. This indicates that there is an incremental thickening of the bilayer by approximately 1 Å when this water model is used. The headgroup peak of the experimental electron density profile of the DPPC bilayer is broader with a maximum at a larger value ($\approx$ 22 Å) than electron density profiles calculated from the simulations. This indicates that the CHARMM36 model underestimate the headgroup–headgroup thickness of DPPC bilayers. The experimental electron density profile for the POPC bilayer shows that the bilayer is incrementally thinner and has a lower maximum than the simulated profiles, although the maximum occurs in a similar position.

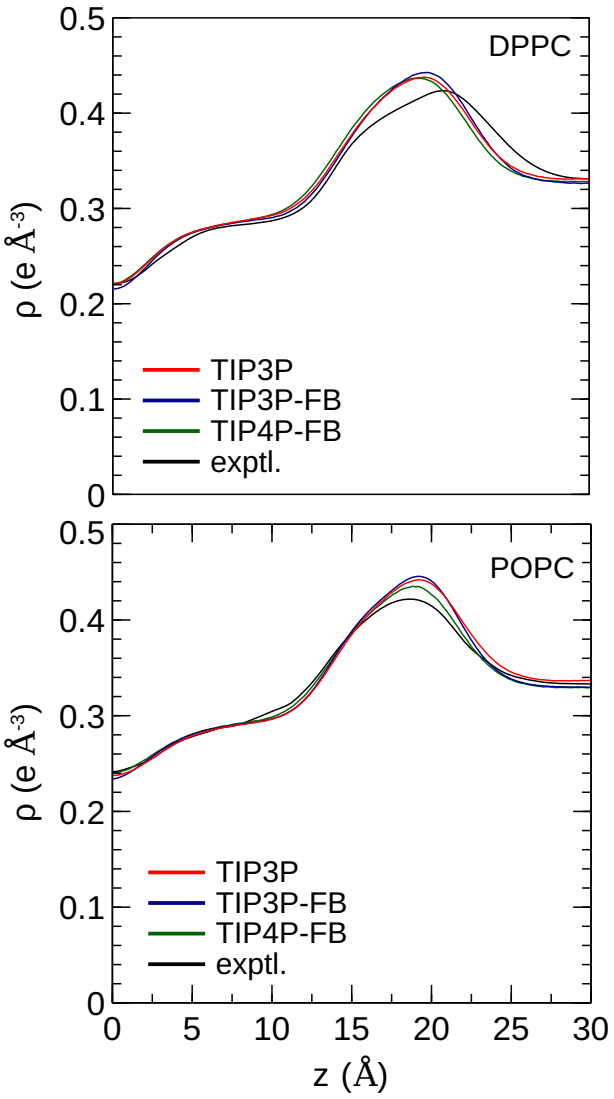

Figure 2.5: Electron density profile for DPPC and POPC bilayers calculated from simulations using the CHARMM36 lipid force field and the three water models. The experimental curves are reproduced from Refs. [67] and [109].

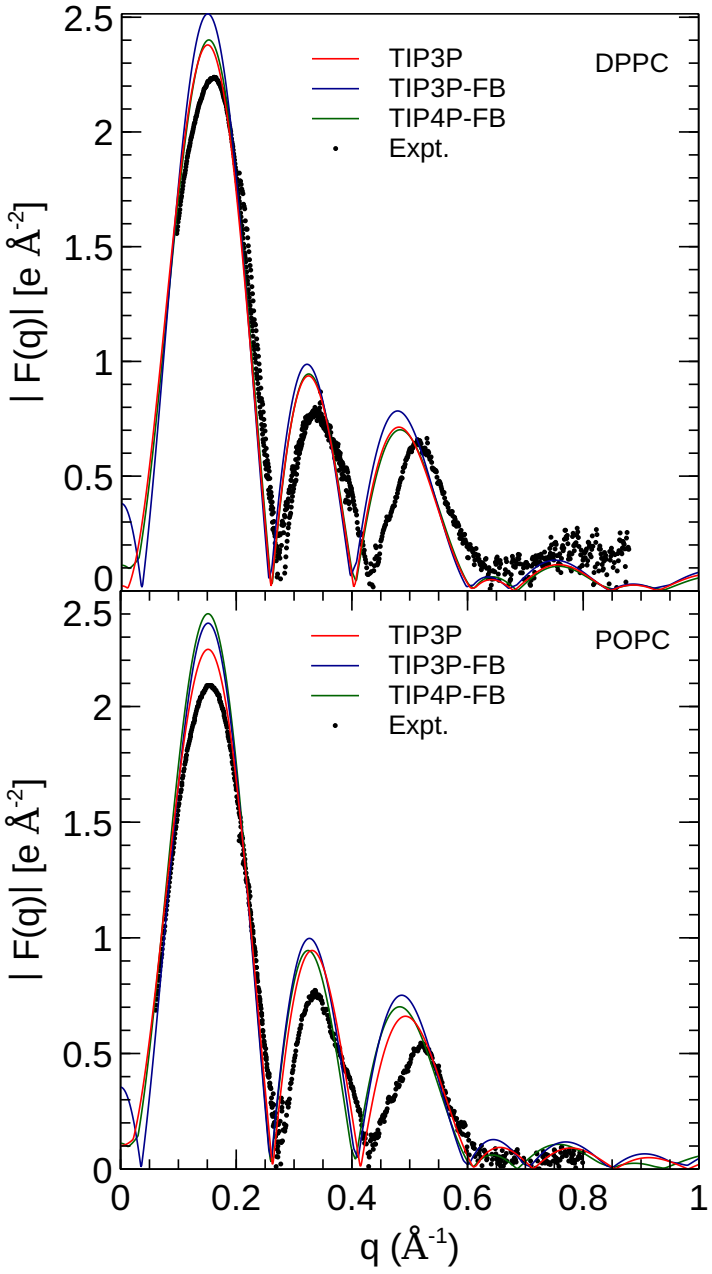

Figure 2.6: X-ray scattering profiles of DPPC (top) and POPC (bottom) lipid bilayers calculated from the simulated electron density profiles. The experimental profile is reproduced from Ref. [68].

The electron density profiles of the two bilayers were transformed into reciprocal space ($F(q)$) so that X-ray scattering curves could be compared directly to the experimental profiles determined from oriented multilayers and unilamellar vesicles [68]. The amplitudes of the scattering form factors ($|F(q)|$) were calculated from the electron density profiles using the relation,

$$|F(q)| = \left| \int_{-L/2}^{L/2} [\rho(z) - \rho_w] \left(\cos(qz) + i \sin(qz)\right) \mathrm{d}z \right| \tag{2.6}$$

where ρ_w is the electron density of the bulk solvent (i.e., water) and q is the z-component of the scattering vector. These curves are presented in Figure 2.6. The curves calculated using all three water models show only subtle differences, consistent with the similar electron density profiles. In comparison to the experimental scattering curves, the positions of the nodes are shifted to incrementally smaller values of q for all three water models and both lipids, but otherwise, all three models are consistent with the X-ray scattering data.

The NSLD profile of a membrane is dominated by the sharp difference in the Neutron Scattering Length (NSL) of protons in the lipids ($a_H = -3.74$ fm) relative to the deuterons of the heavy water solvent ($a_D = 6.67$ fm). As a result, the neutron scattering curve is sensitive to the thickness of the hydrocarbon layer of the bilayer and the depth of penetration of water into the bilayer [68]. The reciprocal-space neutron scattering curves were calculated from the NSL density profiles calculated from the simulations [69]. These curves are presented in Figure 2.7. For both lipid types, the neutron scattering curves calculated using all three models are in good agreement with the experimental scattering curves in the interval where reliable experimental data is available (0.03 Å$^{-1} < q < 0.2$ Å^{-1}). This is consistent with the density profiles, which show only small variations in the bilayer thickness when the water model is changed.

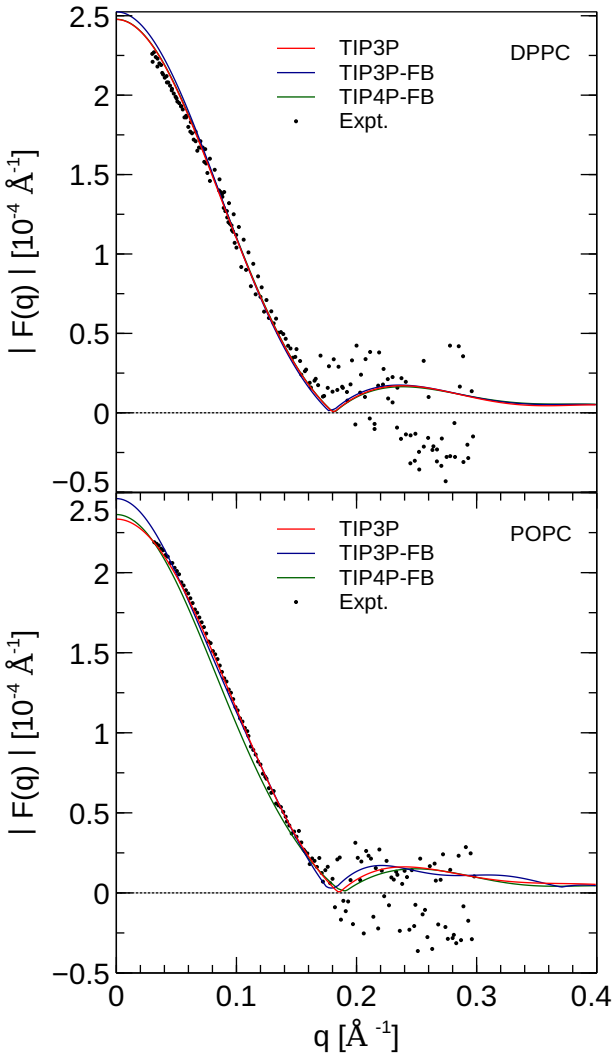

Figure 2.7: Neutron scattering profiles of the lipid bilayers calculated from the simulated neutron scattering length profiles. The experimental profile is reproduced from Ref. [68].

2.4.4 Membrane Dipole Potential

The calculated MDP profiles are presented in Figure 2.8. The membrane dipole potential has not been measured as a function of membrane depth, so the calculated depth-dependent MDP cannot be compared directly to experiment. Experimental estimates of the maximum of the membrane dipole potential are deduced from the relative membrane conductance of hydrophobic cations and anions that have similar radii (e.g., tetraphenylborate vs tetraphenylarsonium) [73]. The conductance is assumed to be limited by the magnitude of the MDP. This experimental maximum is compared to the maxima of the calculated profiles.

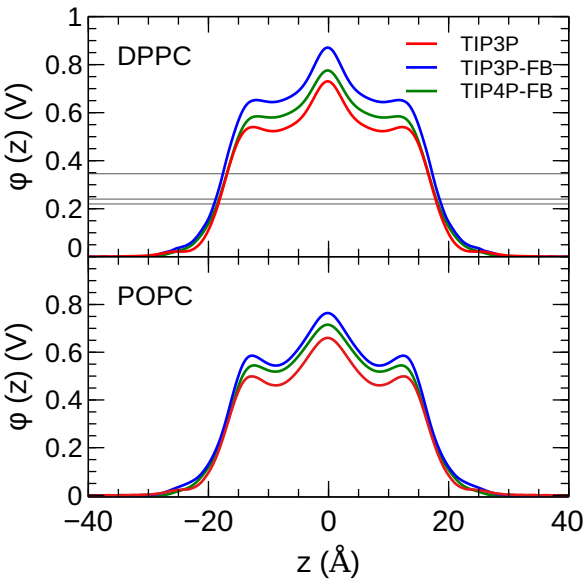

Figure 2.8: The membrane dipole potential (ϕ) calculated for the three water models. The experimental MDP maximums for DPPC from Refs. [110], [111], and [112] are indicated by the gray horizontal lines.

The CHARMM36/mTIP3P force field overestimates the MDP; for DPPC, the maximum of the MDP is 0.73 V, while the experimental estimates range from 0.220 to 0.346 V. High MDPs are also predicted for the CHARMM36/mTIP3P force field. The use of the TIP3P-FB and TIP4P-FB models result in a systematic increase in the

MDP for both the DPPC and POPC bilayers, where the maximum for the MDP is roughly 0.10 V and 0.05 V higher that the mTIP3P potentials, respectively. Most of this difference originates from changes in the electrostatic potential at the lipid–water interface, which is greater when the more polar FB models are used.

2.4.5 Water Permeability

The calculated Gibbs energy profiles and diffusivity profiles of water molecules permeating through the bilayer are presented in Figure 2.9. The water permeabilities of the POPC bilayer calculated using these profiles are presented in Table 2.4.

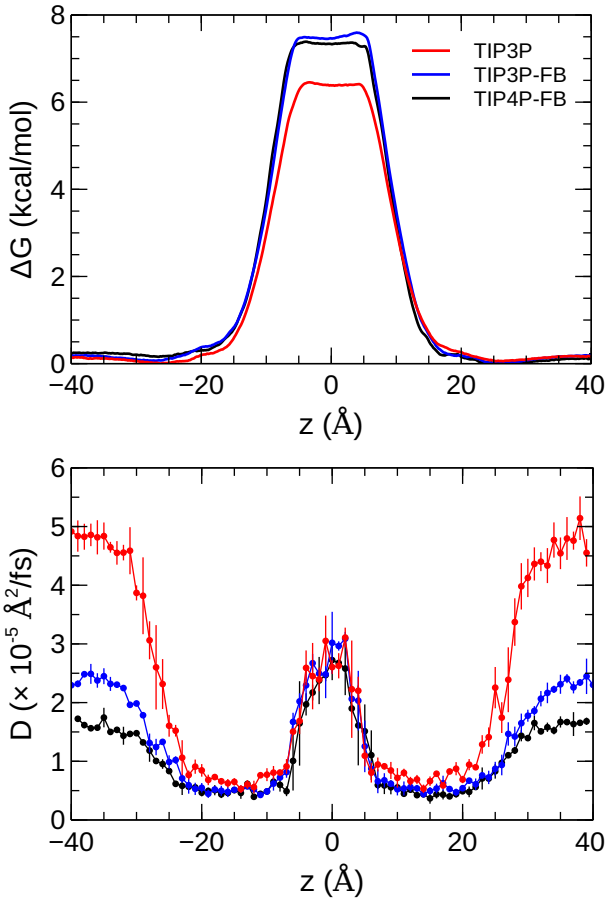

Figure 2.9: The Gibbs energy profile (top) and diffusivity profile (bottom) for a water molecule permeating a pure POPC bilayer at 298 K.

Table 2.4: Water permeability of a pure POPC bilayer using the CHARMM36 lipid force field and the three selected water models. The experimental permeability is taken from Ref. [113].

model	P_m ($\times 10^{-3}$ cm/s)
mTIP3P	4.37 ± 0.03
TIP3P-FB	0.76 ± 0.02
TIP4P-FB	0.88 ± 0.01
expt.	13.0 ± 0.44

The experimental value for the permeability of pure POPC membranes is taken from a study by Mathai et al. [113] In that study, the permeability was measured by subjecting unilamellar vesicles to a 50% increase in osmotic pressure using a stopped-flow device. The volume change of the vesicles due to water permeation in response to the increase in osmotic pressure was determined by measuring the rate of self-quenching of the fluorescence of carboxyfluorescein encapsulated in the vesicle.

The effect of the water model on the diffusivity is apparent in the transmembrane diffusivity profile ($|z| > 20$ Å). The TIP3P water model has a viscosity coefficient that is much lower than the experimental value ($\eta_{TIP3P} = 0.321$ mPa·s vs $\eta_{expt} = 0.896$ mPa·s), so its rate of diffusion in the solution and at the lipid–water interface is unrealistically fast ($D_{H_2O} = 6.05$ cm^2/s). These results are in line with previous simulations [21, 114]. The TIP3P-FB and TIP4P-FB water models have viscosity/self-diffusion coefficients that are much closer to the experimental values, and the diffusivity of the permeating water molecule is lower accordingly. Using these more realistic water models, the water solute diffuses at a faster rate at the center of the bilayer than in solution, opposite to the trend predicted using the mTIP3P model.

The permeabilities predicted by the mTIP3P simulations are in the closest agreement with the experimental value, but still underestimate the permeability by a factor of 3. The solubility–diffusion model used to calculate the membrane permeability is an approximate model, which introduces a source of error. The equation assumes

that there is an equilibrium distribution of the solute across the membrane, although the experiments by Mathai involve a non-equilibrium osmotic pressure increase to induce a flux of water out of the liposome [113]. The solubility–diffusion model also assumes that the z-axis of the simulation cell is an ideal reaction coordinate [21], although undulations and defects in the bilayer cause this approximation to be imperfect [115, 116]. Some reports have suggested that solute permeation through membranes is actually subdiffusive [117], with the membrane interior exhibiting fractional viscosity like long-chain alkanes. This introduces an additional source of error into the simulations.

The force field is another source of inaccuracy, due to limitations of parameterization or the neglect of effects like induced polarization. Notably, the permeability depends exponentially on the height of the Gibbs energy barrier. As a consequence of this, even a small difference in the calculated vs true Gibbs energy barrier would result in a significant difference in predicted permeability. For instance, if the Gibbs energy barrier for permeation of TIP3P-model water was lower by 10%, the predicted permeability would increase by a factor of 2.9. Lee et al. [23] showed that errors of the order of a factor of 10 are typical for membrane permeability calculations. Improved theoretical models, simulation methods, and force fields will be needed to achieve greater accuracy.

The Gibbs energy profile when the permeating water molecule is at the center of the bilayer is 6.4 kcal/mol when the mTIP3P model is used but is approximately 7.4 kcal/mol for the TIP3P-FB and TIP4P-FB models. This can be connected to the Gibbs energy of transfer of a water molecule between liquid water and liquid hexadecane. The model for hexadecane uses the same non-bonded parameters as the aliphatic sections of the lipid chains, making it an appropriate model for the partitioning of a water molecule between the aqueous phase and the center of the

bilayer. The results from the TI/FEP calculation of the Gibbs energy of transfer are presented in Table 2.5. The electrostatic component of the Gibbs energy of transfer is about 1 kcal/mol larger for the TIP3P-FB and TIP4P-FB water models. This larger thermodynamic penalty for transferring a water molecule into hexadecane is consistent with the FB models having higher Gibbs energy profiles of permeation than for the TIP3P model. This ultimately reflects that the TIP3P water model has a smaller excess chemical potential than the TIP3P-FB and TIP4P-FB models (Table 2.6), resulting in a smaller thermodynamic penalty to remove a TIP3P-model water molecule from the aqueous phase. The experimental estimates of $\Delta\mu_{H_2O}$ are consistently lower than those predicted by the TIP3P-FB and TIP4P-FB models. The data for the calculation of the transfer energies are included in Table 2.7.

Table 2.5: Gibbs energy of transfer of one water molecule from liquid water to liquid hexadecane. All values are in units of kcal/mol. The experimental value is taken from Ref. [118].

model	mTIP3P	TIP3P-FB	TIP4P-FB	expt.
electrostatic	8.19 ± 0.06	9.54 ± 0.04	9.45 ± 0.08	
dispersion	-0.68 ± 0.06	-0.89 ± 0.09	-0.82 ± 0.14	
repulsive	0.00 ± 0.38	-0.07 ± 0.50	-0.17 ± 0.41	
total	7.51 ± 0.50	8.58 ± 0.63	8.46 ± 0.63	5.98

Table 2.6: Calculated excess chemical potential of water. Values are in kcal/mol.

model	electrostatic	dispersion	repulsive	total
mTIP3P	-8.41 ± 0.02	-2.72 ± 0.00	4.80 ± 0.05	-6.33 ± 0.07
TIP3P-FB	-9.78 ± 0.02	-2.44 ± 0.00	4.76 ± 0.02	-7.46 ± 0.05
TIP4P-FB	-9.68 ± 0.05	-2.77 ± 0.00	4.95 ± 0.02	-7.50 ± 0.07
expt.			-6.32[a] , -5.74[b]	

[a] Ref. [119], [b] Ref. [120].

Table 2.7: Absolute solvation energy of a water molecule in liquid hexadecane. Values are in kcal/mol.

model	electrostatic	dispersion	repulsive	total
mTIP3P	-0.22 ± 0.04	-3.40 ± 0.06	4.80 ± 0.43	1.18 ± 0.53
TIP3P-FB	-0.24 ± 0.02	-3.33 ± 0.09	4.69 ± 0.52	1.12 ± 0.63
TIP4P-FB	-0.23 ± 0.03	-3.59 ± 0.14	4.78 ± 0.43	0.96 ± 0.60

2.5 Discussion

The calculated headgroup areas and compressibilities showed limited variation with the water model. Experimental values of the headgroup area are typically derived from a combination of estimates of bilayer properties, such as bilayer thickness, volume per lipid, etc. As a result, a wide range of values has been reported for DPPC and POPC lipids [10]. Although the uncertainty in the experimental values makes it difficult to conclude that one water model yields improved headgroup areas and compressibilities, we can conclude that these properties are similar for all three water models and are within the margin of uncertainty of widely-used experimental values.

The calculations of the X-ray and neutron scattering profiles generally indicate that all three water models yield structural distributions that are generally consistent with the experimental form factors, although the nodes of the X-ray scattering profile of the DPPC bilayer are at systematically smaller values of q for all three water models. This suggests that the lipid model would have to be adjusted in order to improve agreement between the simulated profiles and the computationally-predicted profiles because there are only subtle differences in the scattering profiles calculated using the three water models.

Botan et al. [95] had previously showed that the CHARMM36/mTIP3P model was among the most effective force fields for predicting lipid headgroup orientational order parameters. The lipid orientational order parameters calculated from the simulations

presented here were generally insensitive to the water model and were all in reasonable agreement with the experimental values determined using NMR. These data provide some of the more direct measures of the structure of the bilayer, especially at the lipid–water interface, so the success of the models employing the TIP3P-FB and TIP4P-FB water models in calculating orientational order parameters is particularly encouraging. The orientational order parameters of the acyl positions are essentially the same for all three water models.

The membrane dipole potential was overestimated by all models. Simulations with the FB water models overestimate the MDP to an even greater degree than the mTIP3P model. This suggests that the description of the MDP calculated using the CHARMM36 lipid force field cannot be significantly improved by using improved water models. The CHARMM-Drude polarizable force field for lipids predicts more moderate values for the MDP (≈ 0.56 V at the center of the bilayer) [106]. Harder and Roux [72] attributed the improved performance of these polarizable force fields to the polarization of the upper portions of the acyl chains by the water–headgroup interface, which attenuates the increase in the profile in the lipid-headgroup region. This induced polarization effect is not captured by non-polarizable models like CHARMM36; however, the description of other physical properties of the bilayer does not appear to be negatively affected by the neglect of this effect.

The water permeability of a lipid bilayer is notably sensitive to the water model. The rate of permeation of water across a pure POPC bilayer has been measured at 13×10^{-3} cm/s [113], indicating that water molecules are able to cross a membrane at a slow but significant rate. The permeability calculated using the mTIP3P model underestimates this rate by a factor of 3, while the FB models underestimate the rate by a factor of 15–17.

There are several possible explanations for the difference between the permeabilities calculated using the solubility–diffusion model and the experimental values. The factor that affects the rate of permeation most significantly is the height of the barrier in the Gibbs energy profile, which is significantly higher for the FB models than for mTIP3P. All models significantly underestimate the experimental solubility of water in hexadecane, although the FB models overestimate the water–hexadecane transfer energy to a larger degree than the mTIP3P model. These appear to be rooted in the spuriously large excess chemical potentials for the FB models, which we calculated to be −7.46 kcal/mol and −7.50 kcal/mol. In comparison, Shirts et al. showed that the chemical potentials of Simple Point-Charge (SPC), Extended Simple Point Charge model (SPC/E), TIP3P, TIP4P, and TIP4P-Ew ranged from −6.10 kcal/mol to −7.05 kcal/mol, which are closer to the experimental estimates of −5.7 kcal/mol and −6.3 kcal/mol [121]. Limitations of the force field combination rule and neglect of induced polarization have also been proposed to cause the solubility of water in alkane solvents to be underestimated [122, 123]. Reparameterization of the alkane–water non-bonded parameters may be needed to capture the correct water permeability of the bilayer using these models. Because this issue stems specifically from the high excess chemical potential of water in the ForceBalance models, it is unlikely to affect the permeability of other non-ionic solutes, although solutes that permeate with water molecules in complex experience a higher barrier due to the high excess chemical potential.

Piggot et al. [11] observed that simulations of DPPC lipid bilayers in GROMACS using the TIP3P water model and a potential-based switching function resulted in a transition to an ordered phase above the transition temperature for DPPC bilayers.

This issue did not appear in our simulations, which used force-based switching functions in NAMD. Despite our success, Piggot et al.'s results suggest that the TIP3P-FB and TIP4P-FB models should still be used cautiously with the CHARMM36 lipid model because subtle differences in simulation options can result in significant differences in bilayer properties, so our results may not apply when different non-bonded cutoffs, switching options, etc. are used.

2.6 Conclusions

The DPPC and POPC lipid bilayers were simulated using molecular dynamics using the TIP3P-FB and TIP4P-FB water models and compared to the results from simulations using the mTIP3P water model. The headgroup area, compressibility, X-ray and neutron scattering profiles, and acyl-chain orientational order parameters were compared to experimental values. All three models yielded similar results, suggesting that the CHARMM36 model can be used with any of these water models without modification for the simulation of the structure and dynamics of lipid bilayers. This could be advantageous in some instances, as the dielectric constant and viscosity of water simulations using the TIP3P-FB and TIP4P-FB models are closer to the experimental values than when the mTIP3P model is used. The temperature dependent properties of TIP4P-FB model water are significantly better than the mTIP3P and TIP3P-FB models, which could be an advantage in the simulation of temperature dependent properties of water–lipid systems.

More significant differences were apparent in the water permeability of the bilayers. The Gibbs energy profile and diffusivity of a permeating water molecule were calculated along the transmembrane axes and these data were used to calculate the permeability of the bilayer using the solubility–diffusion model. Although this model

is approximate, the TIP3P model was in closer agreement with the experimental estimates than the TIP3P-FB and TIP4P-FB models. This difference stems from the higher Gibbs energy profile when the permeating water molecule is in the middle of the bilayer when the TIP3P-FB and TIP4P-FB water models were used. In turn, this barrier reflects a spuriously low water–alkane partition coefficient for the TIP3P-FB and TIP4P-FB models due to their high excess chemical potentials. This could, in principle, be improved by modifying the water–acyl non-bonded parameters for these models, but this issue is unlikely to be significant for simulations of most of the structural and dynamic properties of lipid bilayers or the permeation of other solutes.

Chapter 3

Modeling the Permeation of Gasotransmitters Through Lipid Bilayers

3.1 Abstract

CO, NO, and H_2S serve as endogenous signaling molecules. Prior experimental and computational studies have shown that NO and H_2S can permeate lipid bilayer membranes at high rates without a facilitator. To provide systematic and consistent predictions on the permeabilities of these three molecules, all-atom molecular dynamics simulations were used to model the permeation of CO, NO, and H_2S through a POPC lipid bilayer. New molecular mechanical models were developed for these three solutes that correctly describe the solvation energy in liquid water and atomic radii consistent with the solvation structure determined using *ab initio* molecular dynamics. The Gibbs energy profiles of permeation through the bilayer were calculated using umbrella sampling. There is no significant Gibbs energy barrier to the permeation of

these molecules through the bilayer and these molecules tend to partition inside the membrane due to their low aqueous solubility. Permeabilities calculated using the solubility–diffusion model are in reasonably good agreement with the experimental values. Simulations with cholesterol-containing membranes indicate a modest effect on the Gibbs energy profiles, but with a net effect of lowering the rate of permeation of NO and H_2S due to a decreased concentration of the gasotransmitters at the center of the bilayer.

3.2 Introduction

CO, NO, and H_2S have been found to serve as endogenous signalling molecules that inhibit their targets by binding to metal centers or through chemical modification of proteins [25]. Through binding to metal centers or chemical modification of proteins, these molecules signal in a wide range of cellular processes, including transcription, apoptosis/proliferation, and inflammatory responses. This has led to the development of probe molecules to observe gasotransmitters in their cellular environments and prodrugs to release gasotransmitters [124, 125].

The mechanism by which gasotransmitters cross cell membranes has been debated. The membranes of some organisms that require high rates of gas transfer are enriched with aquaporins, which are membrane protein channels that allow the selective permeation of water [126]. For example, Lee et al. [34] speculated that hydrogen sulfide permeates through the transmembrane channel AqpM. This aquaporin is present in archaeon *Methanothermobacter marburgensis*, which requires hydrogen sulfide as part of its energy production pathway. Because the selectivity filter of this aquaporin differs from those that only facilitate the passage of water, Lee et al. [113] proposed this channel could also facilitate the permeation of H_2S [34].

Other research has suggested that gasotransmitters can permeate membranes without a facilitator. Subczynski et al. [32] measured the permeability of nitric oxide (NO) through POPC lipid bilayers using Electron Paramagnetic Resonance (EPR) spectroscopy and determined permeability rates of 93 cm/s. Mathai et al. [33] measured the membrane permeability of H_2S through a bilayer composed of reconstituted bacterial lipids at rates greater than 0.5 cm/s. These high rates of permeation suggest that these membranes do not impede the permeation of gasotransmitters, so no protein facilitator is necessary.

Computer simulations have been used extensively to model the permeation of dissolved gases through membranes. Simulations of O_2 permeation have generally predicted these molecules to permeate biological lipid membranes readily [20, 29, 30, 31]. Sugii et al. [35] modeled the permeation of CO and NO and predicted them to permeate at rates similar to O_2. Riahi and Rowley [22] showed that there is only a small barrier on the Gibbs energy profile for the membrane permeation of hydrogen sulfide.

The effect of cholesterol on membrane permeability has also received attention. Generally, the permeability of a membrane decreases by up to 50% as its cholesterol content increases [127, 128, 129, 130, 131, 132]. This trend has also been observed in gasotransmitter permeation; Subczynski found that the permeability coefficient for NO permeation was 17% lower in a POPC bilayer containing 30% cholesterol in comparison to the pure bilayer [32].

The membrane permeability of gasotransmitters has not been investigated systematically using modern simulation methods. Through this study, we hope to provide a quantitatively-accurate model for the permeation of all three gasotransmitters to elucidate their differences and similarities, predict rates of permeation, and compare the results of our simulations to the available experimental data.

3.3 Computational Methods

3.3.1 Permeation Simulations

A simulation cell with a bilayer composed purely of POPC lipids was constructed using CHARMM-GUI [81, 82, 83, 84, 85]. This simulation cell contained 48 POPC lipids and 2611 water molecules. A bilayer containing 30% cholesterol was also constructed, which had a composition of 56 POPC lipids, 24 cholesterol molecules, and 3808 water molecules. A representative simulation cell is illustrated in Figure 3.1. The POPC lipids were represented by the CHARMM36 lipid force field [49]. The cholesterol molecules were represented using the updated version of the CHARMM force field developed by Lim et al. [133] Water molecules were represented using the TIP4P-FB water model [53]. Custom force fields were developed for CO, NO, and H_2S such that the models matched the experimental Gibbs energy of hydration and atomic radii based on *ab initio* molecular dynamics simulations.

All MD simulations were performed using NAMD 2.12 [86]. A 2 fs timestep was used, and bonds containing hydrogen were constrained using the SHAKE algorithm [88]. Electrostatic interactions were calculated using PME electrostatics with a 1 Å grid spacing [87]. The temperature was regulated using a Langevin thermostat with a frequency of 1 ps^{-1}. The pressure was regulated by a Langevin barostat with a period of 100 fs and a relaxation time of 50 fs. CHARMM-style force-based switching functions were used for the Lennard-Jones interactions.

Umbrella sampling simulations were used to calculate the Gibbs energy profiles [54, 55, 134]. In these simulations, the solute was restrained to a position along the z-axis of the simulation cell relative to the center of mass of the lipids. The restraint was a harmonic potential with a spring constant of 2.5 kcal/mol/Å^2. The gasotransmitters were placed at random positions in the plane of the bilayer to generate the

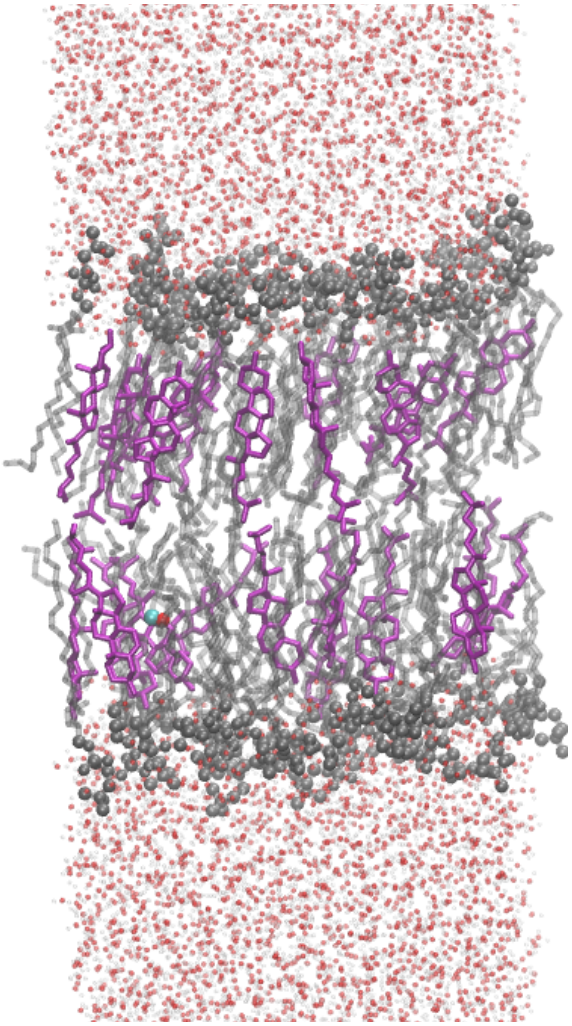

Figure 3.1: Simulation cell for the 70:30 POPC:cholesterol bilayer simulations.

initial configuration of each umbrella sampling window. A 100-cycle minimization was performed on these configurations to eliminate highly-repulsive contacts between atoms placed in close proximity. A 50 ns equilibration was performed for each window, followed by a 200 ns production simulation. This length of simulation has generally been found to be sufficient for the calculation of permeation Gibbs energy profiles for non-ionic solutes [23]. The Gibbs energy profiles were calculated from the umbrella sampling data using WHAM [56, 135].

3.3.2 Parameterization

Calculation of the dispersion coefficients was performed using the eXchange-hole Dipole Moment model (XDM) [136, 137] using the postg postprocessing code [138] based on a geometry-minimized PBE0/aug-cc-pVTZ calculation using Gaussian 09. This density functional method has been shown to provide accurate molecular dipole moments and polarizabilities [139] and provide an *ab initio* basis for dispersion coefficients [140, 141]. The Radial Distribution Functions (RDFs) calculated to determine the atomic radii during the parameterization process were calculated using a 200 ps equilibration simulation followed by a 500 ps sampling simulation. The RDFs of the optimal parameters presented below were calculated using 1 ns equilibration simulations and 2 ns sampling simulations.

TI calculations of the solvation energies were performed using CHARMM c40b2 according to the procedure described by Deng and Roux [60]. A 1 ns equilibration was performed for each window followed by a 1 ns simulation to sample the distribution. The electrostatic and dispersion components were each calculated from 11-window TI simulations with values of λ ranging linearly from 0.0 to 1.0. The repulsive component, corresponding to soft-sphere cavitation energy of the solute, was calculated using a 9-stage FEP simulation. These methods are described in detail in Chapter 1.5.2. The diffusivities of the solutes were calculated from the average of three 5 ns simulations in the microcanonical ensemble after a 1 ns equilibration simulation in the isothermal-isobaric ensemble. Molecular mechanical simulations to calculate the solute RDFs and diffusion coefficients were performed using NAMD 2.12 [86].

3.4 Results and Discussion

3.4.1 Parameterization of Gasotransmitter Models

The optimal Lennard-Jones parameters for the NO, CO, and H_2S models were determined by a grid-search procedure over the Lennard-Jones parameter space. Parameters that yielded atomic radii that matched those determined through *Ab Initio* Molecular Dynamics (AIMD) simulations and that yielded hydration energies that were closest to the experimental values were selected as the optimal parameters. The parameters for these models are presented in Table 3.1.

Table 3.1: Molecular mechanical force field parameters of gasotransmitter models.

solute	parameter	
CO	q_C	-0.0207 e
	$R_{min,C}$	1.7286 Å
	ϵ_C	-0.1682 kcal/mol
	q_O	+0.0207 e
	$R_{min,O}$	1.7766 Å
	ϵ_O	-0.0532 kcal/mol
	k_{C-O}	1115 kcal/mol/Å^2
	$r_{eq,C-O}$	1.128 Å
NO	q_N	-0.0288 e
	$R_{min,N}$	1.507 Å
	ϵ_N	-0.165 kcal/mol
	q_O	+0.0288 e
	$R_{min,O}$	1.4375 Å
	ϵ_O	-0.2015 kcal/mol
	k_{N-O}	763.3 kcal/mol/Å^2
	$r_{eq,N-O}$	1.1508 Å
H_2S	q_S	-0.38 e
	$R_{min,s}$	2.07414 Å
	ϵ_S	-0.46949 kcal/mol
	k_{S-H}	398 kcal/mol/Å^2
	$r_{eq,S-H}$	1.34 Å
	k_{H-S-H}	65.1 kcal/mol/degree^2
	θ_{H-S-H}	92 $^\circ$

The solvation energies of the solute and decomposition into interaction components are presented in Table 3.2. The total hydration energies predicted by the molecular mechanical models are within 1 kJ/mol of the experimental values.

Table 3.2: Solvation energies of gasotransmitters calculated using the molecular mechanical model in comparison to the experimental values. The experimental values are derived from the Henry's law coefficients reported in the National Institute of Standard and Technology (NIST) Webbook. All values are in kJ/mol.

ΔG	CO	NO	H_2S
electrostatic	0.0 ± 0.0	-0.1 ± 0.1	-7.5 ± 0.1
dispersion	-17.2 ± 0.0	-19.3 ± 0.1	-23.6 ± 0.1
repulsive	25.9 ± 0.3	26.4 ± 0.1	29.0 ± 0.3
total	8.7 ± 0.3	7.1 ± 0.1	-2.1 ± 0.2
exptl	9.2	7.6	-2.3

The solvent–solute RDFs calculated using the AIMD and the force fields developed for CO and NO are presented in Figure 3.2, while the RDFs for the H_2S model are presented in Figure 3.3. The location of the first peak of the RDF is consistent with the AIMD values, which was a criterion of our parameterization. The shape of the first minimum and second peak are in reasonable but imperfect agreement with the AIMD values. The limited simulation time and known issues with AIMD predictions of water structure may account for these differences.

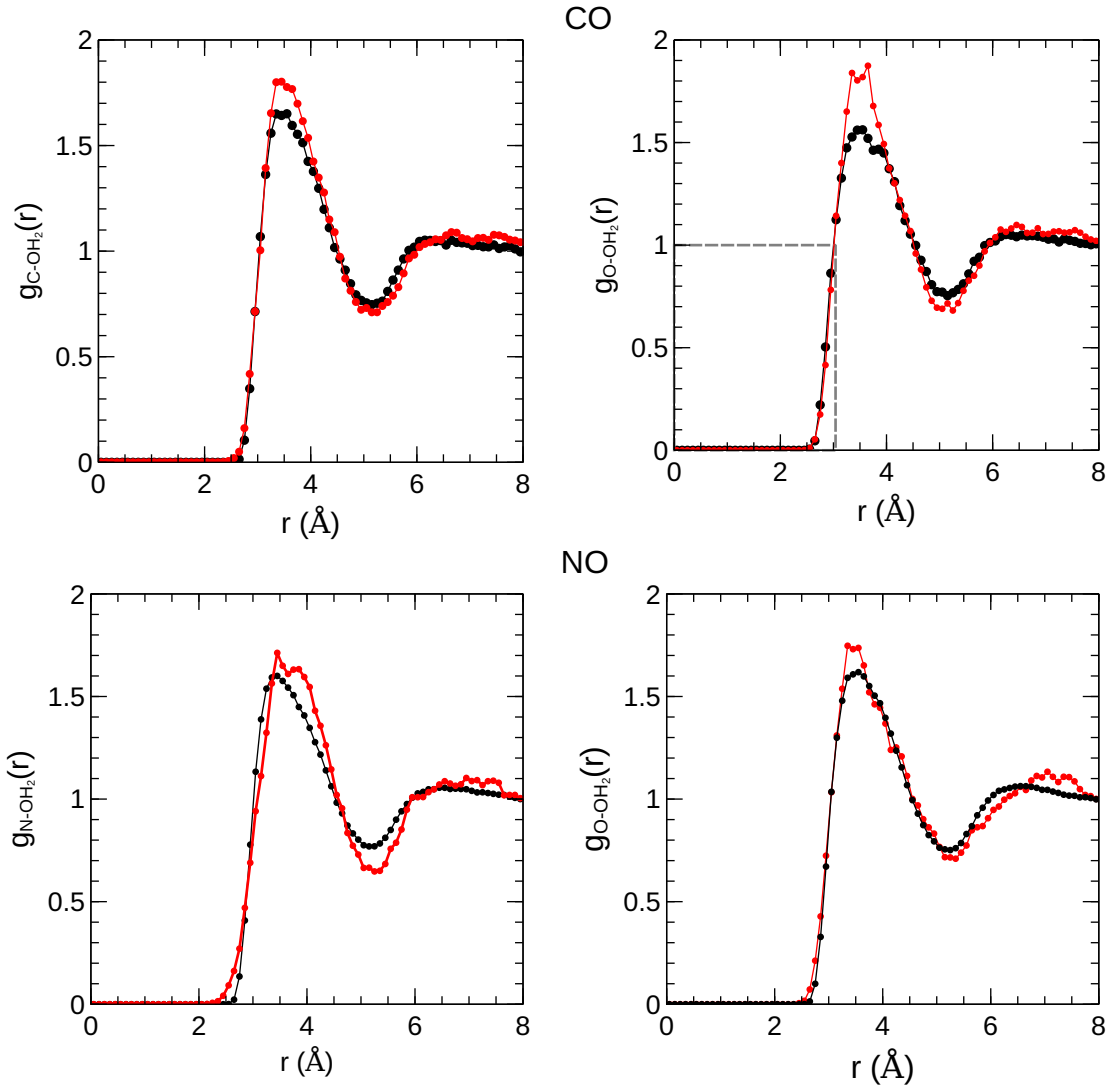

Figure 3.2: RDFs for the interaction of CO (top) and NO (bottom) with water for the force field and ab initio molecular dynamics. The left panels show the distribution of C—OH_2/N—OH_2 distances, while the right panels show the distribution of O—OH_2 distances. The AIMD data for CO is taken from Ref. [142], whereas the AIMD data for NO are from this work. The red line shows the AIMD data while the black line shows RDFs of the optimized molecular mechanical model.

.

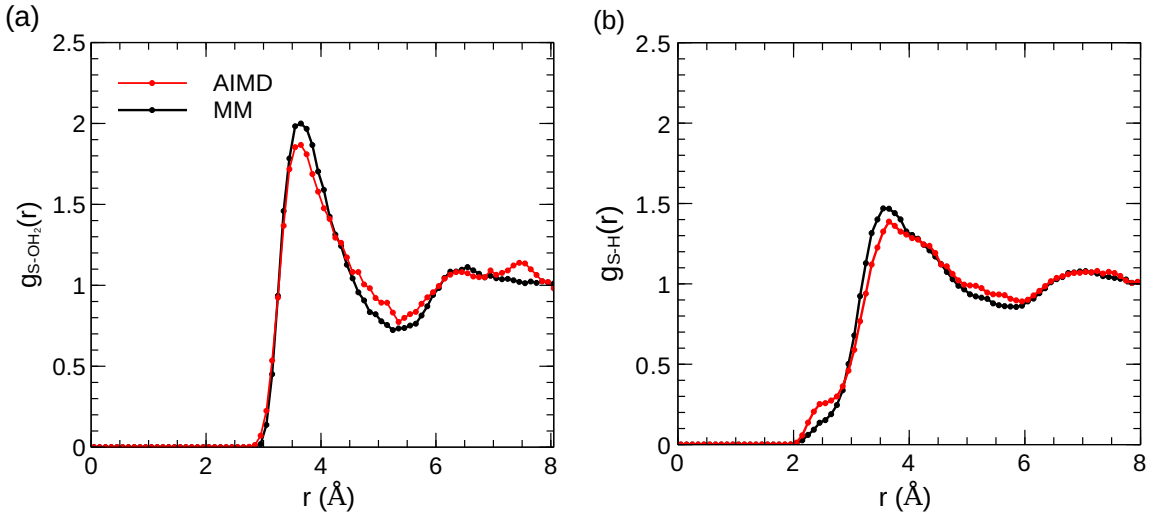

Figure 3.3: RDFs for the interaction of H_2S with water for the force field and *ab initio* molecular dynamics. (a) The RDF for the distance between the S atom of the H_2S and the O atom of H_2O. (b) The RDF for the distance between the S atom of the H_2S and the H atoms of H_2O are shown on the right. The AIMD data (red) for H_2S is taken from Ref. [143]. The RDFs of the MM models are shown in black.

CO is the least soluble ($\Delta G_{solv} = 9.2$ kJ/mol), with NO being incrementally more soluble ($\Delta G_{solv} = 7.6$ kJ/mol). This generally reflects the low polarity of these compounds and their inability to form hydrogen bonds with water. Decomposition of the hydration energy shows that the electrostatic component of this solvation is nearly zero. H_2S is significantly more soluble than either solute, with a modestly-negative solvation energy ($\Delta G_{solv} = -2.1$ kJ/mol). In each case, the calculated Gibbs energy of hydration matches the experimental values within statistical and experimental uncertainty.

3.4.2 Gasotransmitter Permeation

The Gibbs energy profiles for the permeation of CO, NO, and H_2S are presented in Figure 3.4. In each case, the Gibbs energy profile varies only within a 2 kcal/mol range, indicating that the membrane does not present a large barrier to any of these

compounds. In comparison, the permeation of water through a DPPC bilayer has a plateau at the center of the bilayer of roughly 6 kcal/mol [21, 22].

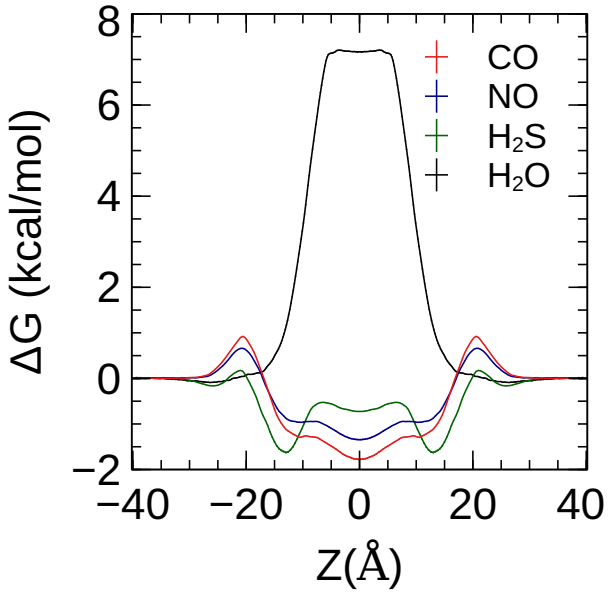

Figure 3.4: Gibbs energy profiles for the permeation of CO, NO, and H_2S through a pure POPC bilayer.

There is a small increase ($<$ 1 kcal/mol) in the Gibbs energy profile in the head-group region (20 Å$<$ $|z|$ $<$ 25 Å) for each gasotransmitter, but the Gibbs energy profile of each permeant becomes negative when the solute is within the bilayer ($|z| <$ 20 Å). This indicates that all three gasotransmitters will spontaneously partition into the interior of the membrane. This Gibbs energy profile shape is typical of small, non-polar solutes [115]. The tendency of NO to concentrate at the centre of a bilayer is consistent with electron paramagnetic resonance (EPR) experiments by Nedeianua et al. [144], who showed that the paramagnetic spin-relaxation enhancement due to NO was the highest for spin labels at the center of a DMPC bilayer.

The Gibbs energy profile of H_2S differs somewhat from those of CO and NO in that its most probable position is in the lipid ester group region (10 Å $<$ $|z|$ $<$ 15 Å) rather than the bilayer centre. This difference can be attributed to the moderate ability of

H_2S to have electrostatic interactions with the ester carbonyls in comparison to the very limited polarity of CO and NO ($\mu_{CO} = 0.112$ D, $\mu_{NO} = 0.153$ D). This profile shape has been reported for polar solutes like chloroform and lidocaine [115, 145].

CO shows the strongest tendency to partition in the center of the bilayer, followed by NO, then H_2S. This order follows the hydrophobicity of these gases, with CO being the least soluble in water and H_2S the most. Although H_2S is more polar than CO and NO, its ability to form hydrogen bonds with water is limited, so it is only sparingly soluble in water [143, 146]. This hydrophobicity favors partitioning of the gasotransmitters from solution to the bilayer interior.

The permeability coefficients of the gasotransmitters were calculated using the solubility–diffusion model (Eqn. 1.2). The calculated values are presented in Table 3.3. The permeability coefficients were estimated by assuming the rates of diffusion of the compounds in the bilayer are equal to the experimental diffusivity in liquid water determined by experiment. Previous simulation studies have shown that the diffusivity of small molecules varies in a limited range during diffusion across the membrane.

Table 3.3: Calculated and experimental permeability coefficients. All values are in units of cm/s.

system	method	CO	NO	H_2S
Pure POPC	calc.	26 ± 4	30 ± 3	38 ± 8
	exptl.	-	93 [a]	$(\geq 0.5 \pm 0.4)$ [b]
70/30 POPC:cholesterol	calc.	26 ± 5	18 ± 4	25 ± 5
	exptl.	-	77 [a]	$(\geq 0.5 \pm 0.4)$ [b]

[a] Ref. [32];
[b] The only experimental value for H_2S permeation is for a bilayer reconstituted from mixed bacterial lipids (Ref. [113]);

The high rates of permeability for these compounds is consistent with Overton's rule [16, 17]. This principle predicts that more hydrophobic solutes will permeate at

faster rates due to their tendency to partition into the bilayer interior. CO shows the strongest tendency to partition in the center of the bilayer, followed by NO, then H_2S. This order follows the hydrophobicity of these gases, with CO being the least soluble in water and H_2S the most. CO, NO, and H_2S are all weakly polar gases that are incapable of forming strong hydrogen bonds with water (Figure 3.5). This low solubility in water results in a tendency to partition into the bilayer readily, resulting in their high membrane permeability.

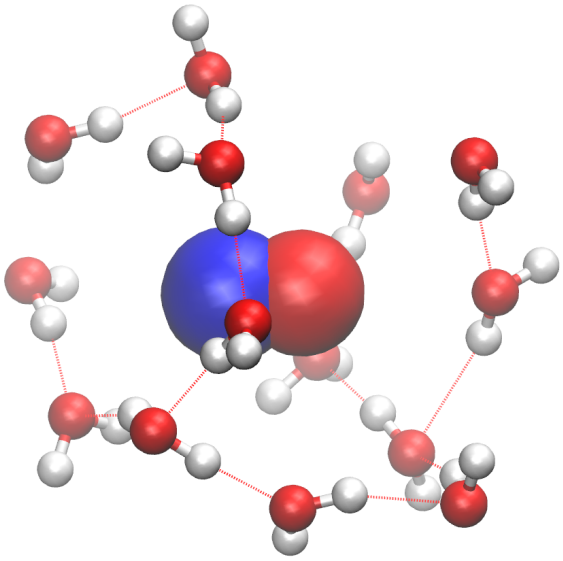

Figure 3.5: Representative configuration of the hydration structure of NO. As a hydrophobic solute, water molecules form a hydrogen-bonded network around the NO.

Although no experimental value for the membrane permeability of CO is available, we predict that it permeates at rates comparable to NO and H_2S. The high membrane permeability appears to be a common feature of gasotransmitters that is distinct from other signaling molecules. As small, hydrophobic molecules, the gasotransmitters can diffuse rapidly in solution and cross membrane barriers readily. Their acute modes of action also provide more immediate signals. This is in contrast to canonical signaling molecules, like hormones or proteins, that act by binding to an extracellular receptor.

3.4.3 Effect of Cholesterol on Permeability

The effect of cholesterol content of the bilayer was investigated by calculating the Gibbs energy profile for permeation of the three gasotransmitters through a 70:30 POPC:cholesterol lipid bilayer (Figure 3.6). For all three gasotransmitters, the Gibbs energy profiles for permeation are slightly lower in the glycerol region but is higher in the lipid tail region in the cholesterol-containing membranes in comparison to the pure POPC membranes. CO and NO are affected to a similar degree, but the increase in profile for H_2S in the tail is systematically about 0.5 kcal/mol higher than for the other two permeants. The calculated permeability coefficients of the cholesterol-containing bilayers show a small net decrease in the permeability of NO and H_2S through cholesterol-containing bilayers, but no net change is observed for CO. The calculated permeability of NO decreases from 30 cm/s to 18 cm/s in the cholesterol-containing membrane. This is consistent with the trend observed by Subczynski using EPR spectroscopy, where the permeability of NO decreased from 93 cm/s in a pure POPC bilayer to 77 cm/s in the 70:30 POPC:cholesterol bilayer [32].

The increase in the Gibbs energy barrier to permeation for cholesterol-containing membranes was also observed in simulations by Wennberg et al., which they attributed to the need for cholesterol and lipids in the bilayer to dissociate in order to allow permeation, weakening the cholesterol–lipid London dispersion interactions [147]. The increase in the Gibbs energy barrier for the permeation of NO through pure POPC vs POPC:cholesterol bilayers is larger than we report here, although the force field and simulation protocol used in our study is different.

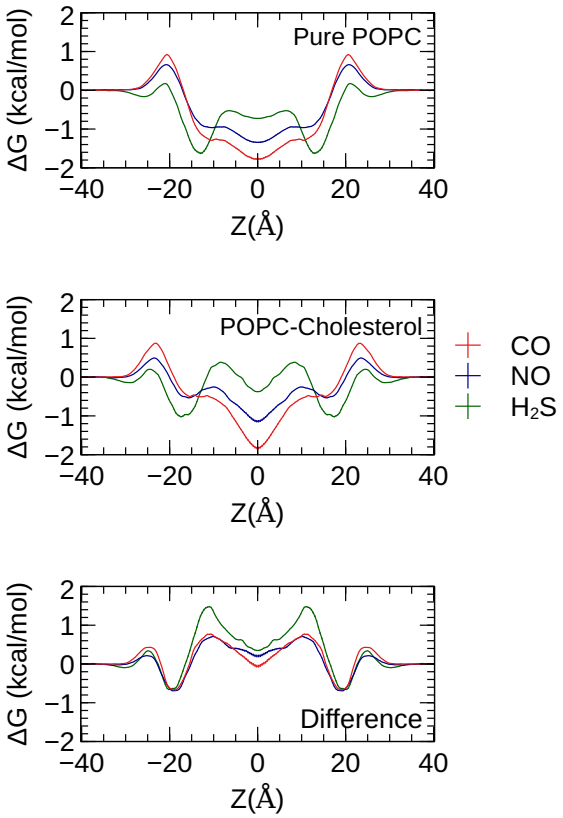

Figure 3.6: Gibbs energy profiles for the permeation of CO, NO, and H_2S through a pure POPC bilayer (top) and a 70:30 POPC:cholesterol bilayer (middle) and their difference (bottom).

3.5 Conclusions

Molecular dynamics simulations were used to model the permeation of the gasotransmitters CO, NO, and H_2S through a pure POPC-lipid bilayer and a POPC lipid bilayer containing 30% cholesterol. The Gibbs energy profiles have low barriers to permeation and indicate a tendency for the gasotransmitters to partition inside the bilayer. CO and NO preferentially partition into the center of the bilayer, while H_2S has increased concentration in the glycerol region.

Permeability coefficients calculated using the inhomogeneous solubility–diffusion model are in reasonably good agreement with the reported experimental values, and

are consistent with rapid unfacilitated passage of these molecules through the bilayer. This work is the first report of the permeability coefficient of CO, which is predicted to permeate at rates of 26 cm/s.

The effect of cholesterol content of the bilayer on the membrane permeability of gasotransmitters was also investigated. The Gibbs energy profiles of permeation through a 70:30 POPC:cholesterol bilayer showed a decrease in solubility at the centre of the membrane but an increase in solubility in the glycerol region. In the computed rates, this resulted in an incremental net decrease in the permeability of NO and H_2S, but the permeability of CO showed no net change.

Chapter 4

Conclusion and Future Work

4.1 Conclusion

In this thesis, molecular simulations were used to understand and predict the permeability of the gasotransmitter molecules NO, CO, and H_2S through model lipid bilayer membranes. In order to achieve a high level of accuracy in the calculations of the rates of permeation, these simulations require accurate molecular mechanical models of the solute, bilayer, and surrounding solution. One limitation of past simulations is that they employ the mTIP3P water model to represent the solution phase because the CHARMM36 lipid model was developed for use with this model. This water model overestimates the dielectric constant and diffusion coefficient of water, which introduce error into the permeation calculations.

In Chapter 2, CHARMM36 lipid force field was shown to be compatible with the TIP3P-FB and TIP4P-FB water models. Simulations of DPPC and POPC bilayers were performed and critical properties of these bilayers were calculated. The calculated headgroup areas, orientational order parameters, and X-ray form factors were in good agreement with the experimental values, which shows that these improved

water models can be used with the CHARMM36 lipid model without modification. These models describe the physical properties of liquid water more realistically than the mTIP3P that is the standard, so this work will allow the water component of lipid–water systems to be modeled more realistically. One drawback of these models is that they have anomalously high excess chemical potentials, so these models predict lower membrane permeabilities than the conventional models.

In Chapter 3, rates of permeation for NO, CO, and H_2S through a pure POPC-lipid bilayer and a POPC lipid bilayer containing 30% cholesterol were calculated using the solubility–diffusion model. The Gibbs energy profiles show a low barrier for permeation of gasotransmitters through the lipid bilayer, showing that these gaseous molecules partition inside the membrane easily. The effect of cholesterol in the bilayer was also explored. The simulations were consistent with the experimental result that solutes permeate cholesterol-containing bilayers as somewhat lower rates than the pure bilayer. In this thesis, we have shown that gasotransmitter molecules, NO, CO, H_2S, permeate lipid bilayer membranes readily. These simulations used the CHARMM36 lipid force field in combination with the TIP4P-FB water model, which was shown in Chapter 2 to be compatible.

4.2 Future Work

The accuracy of permeability simulations could be improved future by more accurate force fields for lipids. Analysis in Chapter 2 indicated that there was some room for improvement in the bilayer scattering profiles, membrane dipole potential, and some orientational order parameters. Validation of force fields non-bonded parameters using QM/MM MD [148, 149, 150, 151, 152], *ab initio* molecular dynamics [142, 153] would help resolve if the non-bonded parameters are appropriate.

One route to improve force fields and explore gasotransmitter permeation would be to calculate the effects of induced polarization. All the simulations reported in this thesis employed a model with fixed atomic charges, although induced polarization could be significant in these simulations because the solute moves from a polar aqueous solution to the non-polar membrane interior [22, 143, 146]. There are polarizable force fields for biomolecules currently available, although the accuracy of these models for calculating structures and energies still require improvement [106, 154, 155].

Additionally, the composition of the membrane could also be varied. In this thesis, simulations were performed simulations on a pure POPC-lipid bilayer and a 70:30 POPC:cholesterol bilayer. Real biological membranes contain a complex mixture of lipids, including polyunsaturated chains, sphingomyelins, phosphatidylserines, and phosphatidylethanolamines [156]. The development of models for these more complex bilayers could allow for simulations of gasotransmitter permeation through lipid bilayers that are better models of real biological membranes.

Bibliography

[1] M. Luckey. *Membrane Structural Biology: With Biochemical and Biophysical Foundations*. Cambridge University Press, 2008.

[2] B. Alberts, A. D. Johnson, J. Lewis, D. Morgan, M. Raff, K. Roberts, and P. Walter. *Molecular Biology of the Cell (Sixth Edition)*. W. W. Norton & Company, 2014.

[3] K. Gaalswyk. Molecular simulation methods for conformational searches and diffusivity. Master's thesis, Memorial University of Newfoundland, 2016.

[4] N. Ridgway and R. McLeod. Functional roles of lipids in membranes. In *Biochemistry of Lipids, Lipoproteins and Membranes*, pages 1–39. Elsevier Science, 2015.

[5] J. Seelig and A. Seelig. Lipid conformation in model membranes and biological membranes. *Q. Rev. Biophys.*, 13(1):19–61, 1980.

[6] O. G. Mouritsen and M. Bloom. Models of lipid-protein interactions in membranes. *Annu. Rev. Biophys. Biomol. Struct.*, 22(1):145–171, 1993.

[7] J. R. Silvius. Role of cholesterol in lipid raft formation: lessons from lipid model systems. *Biochim. Biophys. Acta - Biomembranes*, 1610(2):174–183, 2003.

[8] G. Pabst, M. Rappolt, H. Amenitsch, and P. Laggner. Structural information from multilamellar liposomes at full hydration: Full q-range fitting with high quality x-ray data. *Phys. Rev. E*, 62:4000–4009, 2000.

[9] J. N. Israelachvili. *Intermolecular and Surface Forces*. Academic Press, 3rd edition, 2010.

[10] D. Poger, B. Caron, and A. E. Mark. Validating lipid force fields against experimental data: Progress, challenges and perspectives. *Biochimica et Biophysica Acta (BBA) - Biomembranes*, 1858(7, Part B):1556–1565, 2016.

[11] T. J. Piggot, Á. Piñeiro, and S. Khalid. Molecular dynamics simulations of phosphatidylcholine membranes: A comparative force field study. *J. Chem. Theory Comput.*, 8(11):4593–4609, 2012.

[12] S. P. H. Alexander, A. Mathie, and J. A. Peters. Ion channels. *Br. J. Pharmacol.*, 164(s1):S137–S174, 2001.

[13] B. Thorens and M. Mueckler. Glucose transporters in the 21st century. *Am. J. Physiol. Endocrinol. Metab.*, 298(2):E141–E145, 2010.

[14] A. Walter and J. Gutknecht. Permeability of small nonelectrolytes through lipid bilayer membranes. *J. Membr. Biol.*, 90(3):207–217, 1986.

[15] J. Wijmans and R. Baker. The solution-diffusion model: a review. *Journal of Membrane Science*, 107(1):1 – 21, 1995.

[16] A. Missner, P. Kügler, Y. N. Antonenko, and P. Pohl. Passive transport across bilayer lipid membranes: Overton continues to rule. *Proc. Natl. Acad. Sci. U.S.A.*, 105(52):E123, 2008.

[17] A. Missner and P. Pohl. 110 years of the Meyer–Overton rule: Predicting membrane permeability of gases and other small compounds. *ChemPhysChem*, 10(9-10):1405–1414, 2009.

[18] J. M. Diamond and Y. Katz. Interpretation of nonelectrolyte partition coefficients between dimyristoyl lecithin and water. *J. Membr. Biol.*, 17(1):121–154, 1974.

[19] S.-J. Marrink and H. J. C. Berendsen. Simulation of water transport through a lipid membrane. *J. Phys. Chem.*, 98(15):4155–4168, 1994.

[20] S. J. Marrink and H. J. C. Berendsen. Permeation process of small molecules across lipid membranes studied by molecular dynamics simulations. *J. Phys. Chem.*, 100(41):16729–16738, 1996.

[21] E. Awoonor-Williams and C. N. Rowley. Molecular simulation of nonfacilitated membrane permeation. *Biochimica et Biophysica Acta (BBA) - Biomembranes*, 1858(7, Part B):1672–1687, 2016.

[22] S. Riahi and C. N. Rowley. Why can hydrogen sulfide permeate cell membranes? *J. Am. Chem. Soc.*, 136(43):15111–15113, 2014.

[23] C. T. Lee, J. Comer, C. Herndon, N. Leung, A. Pavlova, R. V. Swift, C. Tung, C. N. Rowley, R. E. Amaro, C. Chipot, Y. Wang, and J. C. Gumbart. Simulation-based approaches for determining membrane permeability of small compounds. *J. Chem. Inf. Model.*, 56(4):721–733, 2016.

[24] C. Szabó. Hydrogen sulphide and its therapeutic potential. *Nat. Rev. Drug Discov.*, 6:917–935, 2007.

[25] A. K. Mustafa, M. M. Gadalla, and S. H. Snyder. Signaling by gasotransmitters. *Sci. Signal.*, 2(68):re2, 2009.

[26] I. Andreadou, E. K. Iliodromitis, T. Rassaf, R. Schulz, A. Papapetropoulos, and P. Ferdinandy. The role of gasotransmitters NO, H_2S and CO in myocardial ischaemia/reperfusion injury and cardioprotection by preconditioning, postconditioning and remote conditioning. *Br. J. Pharmacol.*, 172(6):1587–1606, 2015.

[27] W. K. Subczynski, J. S. Hyde, and A. Kusumi. Oxygen permeability of phosphatidylcholine–cholesterol membranes. *Proc. Natl. Acad. Sci. U.S.A.*, 86(12):4474–4478, 1989.

[28] W. K. Subczynski, L. E. Hopwood, and J. S. Hyde. Is the mammalian cell plasma membrane a barrier to oxygen transport? *J. Gen. Physiol.*, 100:69–87, 1992.

[29] P. Jedlovszky and M. Mezei. Calculation of the free energy profile of H_2O, O_2, CO, CO_2, NO, and $CHCl_3$ in a lipid bilayer with a cavity insertion variant of the Widom method. *J. Am. Chem. Soc.*, 122(21):5125–5131, 2000.

[30] B. G. Dzikovski, V. A. Livshits, and D. Marsh. Oxygen permeation profile in lipid membranes: Comparison with transmembrane polarity profile. *Biophys. J.*, 85(2):1005–1012, 2003.

[31] M. S. Al-Abdul-Wahid, F. Evanics, and R. S. Prosser. Dioxygen transmembrane distributions and partitioning thermodynamics in lipid bilayers and micelles. *Biochemistry*, 50(19):3975–3983, 2011.

[32] W. K. Subczynski, M. Lomnicka, and J. S. Hyde. Permeability of nitric oxide through lipid bilayer membranes. *Free Radical Res.*, 24(5):343–349, 1996.

[33] J. C. Mathai, A. Missner, P. Kügler, S. M. Saparov, M. L. Zeidel, J. K. Lee, and P. Pohl. No facilitator required for membrane transport of hydrogen sulfide. *Proc. Natl. Acad. Sci. U.S.A.*, 106(39):16633–16638, 2009.

[34] J. K. Lee, D. Kozono, J. Remis, Y. Kitagawa, P. Agre, and R. M. Stroud. Structural basis for conductance by the archaeal aquaporin AqpM at 1.68 Å. *Proc. Natl. Acad. Sci. U.S.A.*, 102(52):18932–18937, 2005.

[35] T. Sugii, S. Takagi, and Y. Matsumoto. A molecular-dynamics study of lipid bilayers: Effects of the hydrocarbon chain length on permeability. *J. Chem. Phys.*, 123(18):184714, 2005.

[36] S. E. Feller. Molecular dynamics simulations of lipid bilayers. *Curr. Opin. Colloid Interface Sci.*, 5(3):217–223, 2000.

[37] W. C. Swope, H. C. Andersen, P. H. Berens, and K. R. Wilson. A computer simulation method for the calculation of equilibrium constants for the formation of physical clusters of molecules: Application to small water clusters. *J. Chem. Phys*, 76(1):637–649, 1982.

[38] L. Verlet. Computer "experiments" on classical fluids. I. Thermodynamical properties of Lennard-Jones molecules. *Phys. Rev.*, 159:98–103, 1967.

[39] P. F. Batcho and T. Schlick. Special stability advantages of position-Verlet over velocity-Verlet in multiple-time step integration. *J. Chem. Phys.*, 115(9):4019–4029, 2001.

[40] G. S. Grest and K. Kremer. Molecular dynamics simulation for polymers in the presence of a heat bath. *Phys. Rev. A*, 33:3628–3631, 1986.

[41] G. J. Martyna, D. J. Tobias, and M. L. Klein. Constant pressure molecular dynamics algorithms. *J. Chem. Phys.*, 101(5):4177–4189, 1994.

[42] S. E. Feller, Y. Zhang, R. W. Pastor, and B. R. Brooks. Constant pressure molecular dynamics simulation: The Langevin piston method. *J. Chem. Phys.*, 103(11):4613–4621, 1995.

[43] D. Frenkel and B. Smit. *Understanding Molecular Simulation, Second Edition: From Algorithms to Applications*. Academic Press, Orlando, FL, USA, 2 edition, 2001.

[44] J. Wang, R. M. Wolf, J. W. Caldwell, P. A. Kollman, and D. A. Case. Development and testing of a general amber force field. *J. Comput. Chem.*, 25(9):1157–1174, 2005.

[45] J. E. Jones. On the determination of molecular fields. II. from the equation of state of a gas. *Proc. R. Soc. London, Ser. A*, 106(738):463–477, 1924.

[46] W. F. van Gunsteren, D. Bakowies, R. Baron, I. Chandrasekhar, M. Christen, X. Daura, P. Gee, D. P. Geerke, A. Glättli, P. H. Hnenberger, M. A. Kastenholz, C. Oostenbrink, M. Schenk, D. Trzesniak, N. F. A. van der Vegt, and H. B. Yu. Biomolecular modeling: Goals, problems, perspectives. *Angew. Chem. Int. Ed.*, 45(25):4064–4092, 2006.

[47] D. Poger, W. F. van Gunsteren, and A. E. Mark. A new force field for simulating phosphatidylcholine bilayers. *J. Comput. Chem.*, 31(6):1117–1125, 2010.

[48] J. P. M. Jämbeck and A. P. Lyubartsev. Derivation and systematic validation of a refined all-atom force field for phosphatidylcholine lipids. *J. Phys. Chem. B*, 116(10):3164–3179, 2012.

[49] R. W. Pastor and A. D. MacKerell Jr. Development of the CHARMM force field for lipids. *J. Phys. Chem. Lett.*, 2(13):1526–1532, 2011.

[50] W. L. Jorgensen, J. Chandrasekhar, J. D. Madura, R. W. Impey, and M. L. Klein. Comparison of simple potential functions for simulating liquid water. *J. Chem. Phys.*, 79(2):926–935, 1983.

[51] M. A. González and J. L. F. Abascal. The shear viscosity of rigid water models. *J. Chem. Phys.*, 132(9):096101, 2010.

[52] D. Braun, S. Boresch, and O. Steinhauser. Transport and dielectric properties of water and the influence of coarse-graining: Comparing BMW, SPC/E, and TIP3P models. *J. Chem. Phys.*, 140(6):064107, 2014.

[53] L.-P. Wang, T. J. Martinez, and V. S. Pande. Building force fields: An automatic, systematic, and reproducible approach. *J. Phys. Chem. Lett.*, 5(11):1885–1891, 2014.

[54] G. M. Torrie and J. P. Valleau. Nonphysical sampling distributions in Monte Carlo free-energy estimation: Umbrella sampling. *J. Comput. Phys.*, 23:187–199, 1977.

[55] B. Roux. The calculation of the potential of mean force using computer simulations. *Comput. Phys. Commun.*, 91(1–3):275–282, 1995.

[56] S. Kumar, J. M. Rosenberg, D. Bouzida, R. H. Swendsen, and P. A. Kollman. The weighted histogram analysis method for free-energy calculations on biomolecules. I. The method. *J. Comput. Chem.*, 13(8):1011–1021, 1992.

[57] T. P. Straatsma and H. J. C. Berendsen. Free energy of ionic hydration: Analysis

of a thermodynamic integration technique to evaluate free energy differences by molecular dynamics simulations. *J. Chem. Phys.*, 89(9):5876–5886, 1988.

[58] R. W. Zwanzig. High-temperature equation of state by a perturbation method. I. Nonpolar gases. *J. Chem. Phys.*, 22(8):1420–1426, 1954.

[59] J. D. Weeks, D. Chandler, and H. C. Andersen. Role of repulsive forces in determining the equilibrium structure of simple liquids. *J. Chem. Phys.*, 54(12):5237–5247, 1971.

[60] Y. Deng and B. Roux. Hydration of amino acid side chains: Nonpolar and electrostatic contributions calculated from staged molecular dynamics free energy simulations with explicit water molecules. *J. Phys. Chem. B*, 108(42):16567–16576, 2004.

[61] N. Metropolis, A. W. Rosenbluth, M. N. Rosenbluth, A. H. Teller, and E. Teller. Equation of state calculations by fast computing machines. *J. Chem. Phys.*, 21(6):1087–1092, 1953.

[62] C. J. Woods, J. W. Essex, and M. A. King. The development of replica-exchange-based free-energy methods. *J. Phys. Chem. B*, 107(49):13703–13710, 2003.

[63] W. Jiang, J. Phillips, L. Huang, M. Fajer, Y. Meng, J. C. Gumbart, Y. Luo, K. Schulten, and B. Roux. Generalized scalable multiple copy algorithms for molecular dynamics simulations in NAMD. *Computer Phys. Comm.*, 185:908–916, 2014.

[64] O. Berger, O. Edholm, and F. Jähnig. Molecular dynamics simulations of a fluid bilayer of dipalmitoylphosphatidylcholine at full hydration, constant pressure, and constant temperature. *Biophys. J.*, 72(5):2002–2013, 1997.

[65] B. A. Lewis and D. M. Engelman. Lipid bilayer thickness varies linearly with acyl chain length in fluid phosphatidylcholine vesicles. *J. Mol. Biol.*, 166(2):211–217, 1983.

[66] J. F. Nagle and S. Tristram-Nagle. Structure of lipid bilayers. *Biochimica et Biophysica Acta (BBA) - Reviews on Biomembranes*, 1469(3):159–195, 2000.

[67] N. Kučerka, S. Tristram-Nagle, and J. F. Nagle. Closer look at structure of fully hydrated fluid phase DPPC bilayers. *Biophys J.*, 90(11):L83–L85, 2006.

[68] N. Kučerka, J. F. Nagle, J. N. Sachs, S. E. Feller, J. Pencer, A. Jackson, and J. Katsaras. Lipid bilayer structure determined by the simultaneous analysis of neutron and x-ray scattering data. *Biophys. J.*, 95(5):2356–2367, 2008.

[69] N. Kučerka, J. Katsaras, and J. F. Nagle. Comparing membrane simulations to scattering experiments: Introducing the SIMtoEXP software. *J. Membr. Biol.*, 235(1):43–50, 2010.

[70] N. Kučerka, M.-P. Nieh, and J. Katsaras. Fluid phase lipid areas and bilayer thicknesses of commonly used phosphatidylcholines as a function of temperature. *Biochimica et Biophysica Acta (BBA) - Biomembranes*, 1808(11):2761–2771, 2011.

[71] L. S. Vermeer, B. L. de Groot, V. Réat, A. Milon, and J. Czaplicki. Acyl chain order parameter profiles in phospholipid bilayers: computation from molecular dynamics simulations and comparison with 2H NMR experiments. *Eur. Biophys. J.*, 36(8):919–931, 2007.

[72] E. Harder, A. D. MacKerell, Jr., and B. Roux. Many-body polarization effects and the membrane dipole potential. *J. Am. Chem. Soc.*, 131(8):2760–2761, 2009.

[73] L. Wang. Measurements and implications of the membrane dipole potential. *Annu. Rev. Biochem.*, 81(1):615–635, 2012.

[74] J. C. Gumbart, I. Teo, B. Roux, and K. Schulten. Reconciling the roles of kinetic and thermodynamic factors in membrane–protein insertion. *J. Am. Chem. Soc.*, 135(6):2291–2297, 2013.

[75] M. Orsi and J. W. Essex. Chapter 4 Passive permeation across lipid bilayers: A literature review. In *Molecular Simulations and Biomembranes: From Biophysics to Function*, pages 76–90. The Royal Society of Chemistry, 2010.

[76] E. Brini, C. J. Fennell, M. Fernandez-Serra, B. Hribar-Lee, M. Lukšič, and K. A. Dill. How water's properties are encoded in its molecular structure and energies. *Chem. Rev.*, 117(19):12385–12414, 2017.

[77] A. V. Onufriev and S. Izadi. Water models for biomolecular simulations. *WIREs Comput Mol Sci*, 8(2):e1347, 2017.

[78] C. Vega, J. L. F. Abascal, and I. Nezbeda. Vapor-liquid equilibria from the triple point up to the critical point for the new generation of TIP4P-like models: TIP4P/Ew, TIP4P/2005, and TIP4P/ice. *J. Chem. Phys.*, 125(3):034503, 2006.

[79] M. Javanainen, A. Lamberg, L. Cwiklik, I. Vattulainen, and O. H. S. Ollila. Atomistic model for nearly quantitative simulations of Langmuir monolayers. *Langmuir*, 34(7):2565–2572, 2018.

[80] S. Izadi, R. Anandakrishnan, and A. V. Onufriev. Building water models: A different approach. *J. Phys. Chem. Lett.*, 5(21):3863–3871, 2014.

[81] S. Jo, T. Kim, V. G. Iyer, and W. Im. CHARMM-GUI: A web-based graphical user interface for CHARMM. *J. Comput. Chem.*, 29(11):1859–1865, 2008.

[82] S. Jo, T. Kim, and W. Im. Automated builder and database of protein/membrane complexes for molecular dynamics simulations. *PLoS One*, 2(9):1–9, 2007.

[83] S. Jo, J. B. Lim, J. B. Klauda, and W. Im. CHARMM-GUI membrane builder for mixed bilayers and its application to yeast membranes. *Biophys. J.*, 97(1):50–58, 2009.

[84] E. L. Wu, X. Cheng, S. Jo, H. Rui, K. C. Song, E. M. DvilaContreras, Y. Qi, J. Lee, V. MonjeGalvan, R. M. Venable, J. B. Klauda, and W. Im. CHARMMGUI membrane builder toward realistic biological membrane simulations. *J. Comput. Chem.*, 35(27):1997–2004, 2014.

[85] J. Lee, X. Cheng, J. M. Swails, M. S. Yeom, P. K. Eastman, J. A. Lemkul, S. Wei, J. Buckner, J. C. Jeong, Y. Qi, S. Jo, V. S. Pande, D. A. Case, C. L. Brooks, A. D. MacKerell, J. B. Klauda, and W. Im. CHARMM-GUI input generator for NAMD, GROMACS, AMBER, OpenMM, and CHARMM/OpenMM simulations using the CHARMM36 additive force field. *J. Chem. Theory. Comput.*, 12(1):405–413, 2016.

[86] J. C. Phillips, R. Braun, W. Wang, J. Gumbart, E. Tajkhorshid, E. Villa, C. Chipot, R. D. Skeel, L. Kalé, and K. Schulten. Scalable molecular dynamics with NAMD. *J. Comput. Chem.*, 26(16):1781–1802, 2005.

[87] T. Darden, D. York, and L. Pedersen. Particle mesh Ewald: An N · log(N) method for Ewald sums in large systems. *J. Chem. Phys.*, 98(12):10089–10092, 1993.

[88] J.-P. Ryckaert, G. Ciccotti, and H. J. C. Berendsen. Numerical integration

of the Cartesian equations of motion of a system with constraints: molecular dynamics of n-alkanes. *J. Comput. Phys.*, 23(3):327–341, 1977.

[89] S. R. Durell, B. R. Brooks, and A. Ben-Naim. Solvent-induced forces between two hydrophilic groups. *J. Phys. Chem.*, 98(8):2198–2202, 1994.

[90] E. Neria, S. Fischer, and M. Karplus. Simulation of activation free energies in molecular systems. *J. Chem. Phys.*, 105(5):1902–1921, 1996.

[91] T. Giorgino. Computing 1-D atomic densities in macromolecular simulations: The density profile tool for VMD. *Comput. Phys. Commun.*, 185(1):317–322, 2014.

[92] R. W. Benz, F. Castro-Román, D. J. Tobias, and S. H. White. Experimental validation of molecular dynamics simulations of lipid bilayers: A new approach. *Biophys. J.*, 88(2):805–817, 2005.

[93] R. Guixà-González, I. Rodriguez-Espigares, J. M. Ramrez-Anguita, P. Carrió-Gaspar, H. Martinez-Seara, T. Giorgino, and J. Selent. MEMBPLUGIN: studying membrane complexity in VMD. *Bioinformatics*, 30(10):1478–1480, 2014.

[94] W. Humphrey, A. Dalke, and K. Schulten. VMD: visual molecular dynamics. *J. Mol. Graph.*, 14:33–38, 1996.

[95] A. Botan, F. Favela-Rosales, P. F. J. Fuchs, M. Javanainen, M. Kanduv, W. Kulig, A. Lamberg, C. Loison, A. Lyubartsev, M. S. Miettinen, L. Monticelli, J. Määttä, O. H. S. Ollila, M. Retegan, T. Róg, H. Santuz, and J. Tynkkynen. Toward atomistic resolution structure of phosphatidylcholine headgroup and glycerol backbone at different ambient conditions. *J. Phys. Chem. B*, 119(49):15075–15088, 2015.

[96] J. N. Sachs, P. S. Crozier, and T. B. Woolf. Atomistic simulations of biologically realistic transmembrane potential gradients. *J. Chem. Phys.*, 121(22):10847–10851, 2004.

[97] C. Neale, W. D. Bennett, D. P. Tieleman, and R. Pomès. Statistical convergence of equilibrium properties in simulations of molecular solutes embedded in lipid bilayers. *J. Chem. Theory Comput.*, 7:4175–4188, 2011.

[98] N. Nitschke, K. Atkovska, and J. S. Hub. Accelerating potential of mean force calculations for lipid membrane permeation: System size, reaction coordinate, solute-solute distance, and cutoffs. *J. Chem. Phys.*, 145(12):125101, 2016.

[99] A. Grossfield. WHAM: the weighted histogram analysis method, version 2.0.6, http://membrane.urmc.rochester.edu/content/wham, 2018.

[100] G. Hummer. Position-dependent diffusion coefficients and free energies from bayesian analysis of equilibrium and replica molecular dynamics simulations. *New J. Phys.*, 7:34, 2005.

[101] K. Gaalswyk, E. Awoonor-Williams, and C. N. Rowley. Generalized Langevin methods for calculating transmembrane diffusivity. *J. Chem. Theory. Comput.*, 12(11):5609–5619, 2016.

[102] H. Binder and K. Gawrisch. Effect of unsaturated lipid chains on dimensions, molecular order and hydration of membranes. *J. Phys. Chem. B*, 105(49):12378–12390, 2001.

[103] A. Seelig and J. Seelig. Dynamic structure of fatty acyl chains in a phospholipid bilayer measured by deuterium magnetic resonance. *Biochemistry*, 13(23):4839–4845, 1974.

[104] J. Seelig and N. Waespe-Sarcevic. Molecular order in cis and trans unsaturated phospholipid bilayers. *Biochemistry*, 17(16):3310–3315, 1978.

[105] J. P. Douliez, A. Léonard, and E. J. Dufourc. Restatement of order parameters in biomembranes: calculation of C–C bond order parameters from C–D quadrupolar splittings. *Biophys J.*, 68(5):1727–1739, 1995.

[106] H. Li, J. Chowdhary, L. Huang, X. He, A. D. MacKerell, and B. Roux. Drude polarizable force field for molecular dynamics simulations of saturated and unsaturated zwitterionic lipids. *J. Chem. Theory Comput.*, 13(9):4535–4552, 2017.

[107] H. U. Gally, W. Niederberger, and J. Seelig. Conformation and motion of the choline head group in bilayers of dipalmitoyl-3-sn-phosphatidylcholine. *Biochemistry*, 14(16):3647–3652, 1975.

[108] T. M. Ferreira, F. Coreta-Gomes, O. H. S. Ollila, M. J. Moreno, W. L. C. Vaz, and D. Topgaard. Cholesterol and POPC segmental order parameters in lipid membranes: solid state 1H13C NMR and MD simulation studies. *Phys. Chem. Chem. Phys.*, 15:1976–1989, 2013.

[109] N. Kučerka, S. Tristram-Nagle, and J. Nagle. Structure of fully hydrated fluid phase lipid bilayers with monounsaturated chains. *J. Membr. Biol.*, 208(3):193–202, 2006.

[110] K. Gawrisch, D. Ruston, J. Zimmerberg, V. A. Parsegian, R. P. Rand, and N. Fuller. Membrane dipole potentials, hydration forces, and the ordering of water at membrane surfaces. *Biophys. J.*, 61(5):1213–1223, 1992.

[111] J. Schamberger and R. J. Clarke. Hydrophobic ion hydration and the magnitude of the dipole potential. *Biophys. J.*, 82(6):3081–3088, 2002.

[112] U. Peterson, D. A. Mannock, R. N. A. H. Lewis, P. Pohl, R. N. McElhaney, and E. E. Pohl. Origin of membrane dipole potential: Contribution of the phospholipid fatty acid chains. *Chem. Phys. Lipids*, 117(1):19–27, 2002.

[113] J. C. Mathai, S. Tristram-Nagle, J. F. Nagle, and M. L. Zeidel. Structural determinants of water permeability through the lipid membrane. *J. Gen. Phys.*, 131(1):69–76, 2008.

[114] B. B. Issack and G. H. Peslherbe. Effects of cholesterol on the thermodynamics and kinetics of passive transport of water through lipid membranes. *J. Phys. Chem. B*, 119(29):9391–9400, 2015.

[115] C. Neale and R. Pomès. Sampling errors in free energy simulations of small molecules in lipid bilayers. *Biochimica et Biophysica Acta (BBA) - Biomembranes*, 1858(10):2539–2548, 2016.

[116] W. F. D. Bennett and D. P. Tieleman. The importance of membrane defects – lessons from simulations. *Acc. Chem. Res.*, 47(8):2244–2251, 2014.

[117] C. Chipot and J. Comer. Subdiffusion in membrane permeation of small molecules. *Sci. Rep.*, 6:35913, 2016.

[118] M. H. Abraham, G. S. Whiting, R. Fuchs, and E. J. Chambers. Thermodynamics of solute transfer from water to hexadecane. *J. Chem. Soc., Perkin Trans. 2*, pages 291–300, 1990.

[119] A. Ben-Naim and Y. Marcus. Solvation thermodynamics of nonionic solutes. *J. Chem. Phys.*, 81(4):2016–2027, 1984.

[120] J. Hermans, A. Pathiaseril, and A. Anderson. Excess free energy of liquids from

molecular dynamics simulations. Application to water models. *J. Am. Chem. Soc.*, 110(18):5982–5986, 1988.

[121] M. R. Shirts and V. S. Pande. Solvation free energies of amino acid side chain analogs for common molecular mechanics water models. *J. Chem. Phys.*, 122(13):134508, 2005.

[122] D. Ballal, P. Venkataraman, W. A. Fouad, K. R. Cox, and W. G. Chapman. Isolating the non-polar contributions to the intermolecular potential for water-alkane interactions. *J. Chem. Phys.*, 141(6):064905, 2014.

[123] J. G. McDaniel and A. Yethiraj. Comment on isolating the non-polar contributions to the intermolecular potential for water–alkane interactions [J. Chem. Phys. 141, 064905 (2014)]. *J. Chem. Phys.*, 144(13):137101, 2016.

[124] R. Motterlini and L. E. Otterbein. The therapeutic potential of carbon monoxide. *Nat. Rev. Drug Discov.*, 9:728–743, 2010.

[125] U. Schatzschneider. Novel lead structures and activation mechanisms for CO-releasing molecules (CORMs). *Br. J. Pharmacol.*, 172(6):1638–1650, 2015.

[126] G. V. R. Prasad, L. A. Coury, F. Finn, and M. L. Zeidel. Reconstituted aquaporin 1 water channels transport CO_2 across membranes. *J. Biol. Chem.*, 273(50):33123–33126, 1998.

[127] A. Finkelstein and A. Cass. Effect of cholesterol on the water permeability of thin lipid membranes. *Nature*, 216:717–718, 1967.

[128] R. N. McElhaney, J. D. Gier, and L. L. M. V. Deenen. The effect of alterations

in fatty acid composition and cholesterol content on the permeability of Mycoplasma laidlawii b cells and derived liposomes. *Biochimica et Biophysica Acta (BBA) - Biomembranes*, 219(1):245–247, 1970.

[129] D. Papahadjopoulos, S. Nir, and S. Ohki. Permeability properties of phospholipid membranes: Effect of cholesterol and temperature. *Biochimica et Biophysica Acta (BBA) - Biomembranes*, 266(3):561–583, 1972.

[130] K. Korten, T. J. Sommer, and K. W. Miller. Membrane composition modulates thiopental partitioning in bilayers and biomembranes. *Biochimica et Biophysica Acta (BBA) - Biomembranes*, 599(1):271–279, 1980.

[131] R. A. Smith, E. G. Porter, and K. W. Miller. The solubility of anesthetic gases in lipid bilayers. *Biochimica et Biophysica Acta (BBA) - Biomembranes*, 645(2):327–338, 1981.

[132] W. K. Subczynski, A. Wisniewska, J.-J. Yin, J. S. Hyde, and A. Kusumi. Hydrophobic barriers of lipid bilayer membranes formed by reduction of water penetration by alkyl chain unsaturation and cholesterol. *Biochemistry*, 33(24):7670–7681, 1994.

[133] J. B. Lim, B. Rogaski, and J. B. Klauda. Update of the cholesterol force field parameters in CHARMM. *J. Phys. Chem. B*, 116(1):203–210, 2012.

[134] J. Kästner. Umbrella sampling. *Wiley Interdiscip. Rev. Comput. Mol. Sci.*, 1(6):932–942, 2011.

[135] M. R. Shirts and J. D. Chodera. Statistically optimal analysis of samples from multiple equilibrium states. *J. Chem. Phys.*, 129(12):124105, 2008.

[136] A. D. Becke and E. R. Johnson. A density-functional model of the dispersion interaction. *J. Chem. Phys.*, 123(15), 2005.

[137] A. D. Becke and E. R. Johnson. Exchange-hole dipole moment and the dispersion interaction revisited. *J. Chem. Phys.*, 127(15):154108, 2007.

[138] E. Johnson. Postg. http://schooner.chem.dal.ca, 2018. (accessed June 5, 2018).

[139] A. L. Hickey and C. N. Rowley. Benchmarking quantum chemical methods for the calculation of molecular dipole moments and polarizabilities. *J. Phys. Chem. A*, 118(20):3678–3687, 2014.

[140] M. Mohebifar, E. R. Johnson, and C. N. Rowley. Evaluating force-field London dispersion coefficients using the exchange-hole dipole moment model. *J. Chem. Theor. Comput.*, 13(12):6146–6157, 2017.

[141] E. T. Walters, M. Mohebifar, E. R. Johnson, and C. N. Rowley. Evaluating the London dispersion coefficients of protein force fields using the exchange-hole dipole moment model. *J. Phys. Chem. B*, 122(26):6690–6701, 2018.

[142] E. Awoonor-Williams and C. N. Rowley. The hydration structure of carbon monoxide by ab initio methods. *J. Chem. Phys.*, 146(3):034503, 2017.

[143] S. Riahi and C. N. Rowley. Solvation of hydrogen sulfide in liquid water and at the water–vapor interface using a polarizable force field. *J. Phys. Chem. B*, 118(5):1373–1380, 2014.

[144] S. Nedeianu, T. Páli, and D. Marsh. Membrane penetration of nitric oxide and its donor S-nitroso-N-acetylpenicillamine: a spin-label electron paramagnetic resonance spectroscopic study. *Biochim. Biophys. Acta - Biomembranes*, 1661(2):135–143, 2004.

[145] J. P. M. Jämbeck and A. P. Lyubartsev. Exploring the free energy landscape of solutes embedded in lipid bilayers. *J. Phys. Chem. Lett.*, 4(11):1781–1787, 2013.

[146] S. Riahi and C. N. Rowley. A Drude polarizable model for liquid hydrogen sulfide. *J. Phys. Chem. B*, 117(17):5222–5229, 2013.

[147] C. L. Wennberg, D. van der Spoel, and J. S. Hub. Large influence of cholesterol on solute partitioning into lipid membranes. *J. Am. Chem. Soc*, 134(11):5351–5361, 2012.

[148] C. N. Rowley and T. K. Woo. Counteranion effects on the zirconocene polymerization catalyst olefin complex from QM/MM molecular dynamics simulations. *Organometallics*, 30(8):2071–2074, 2011.

[149] S. Riahi and C. N. Rowley. The CHARMM–TURBOMOLE interface for efficient and accurate QM/MM molecular dynamics, free energies, and excited state properties. *J. Comput. Chem.*, 35(28):2076–2086, 2014.

[150] S. Riahi, B. Roux, and C. N. Rowley. QM/MM molecular dynamics simulations of the hydration of Mg(II) and Zn(II) ions. *Can J. Chem.*, 91(7):552–558, 2013.

[151] C. N. Rowley and B. Roux. The solvation structure of Na^+ and K^+ in liquid water determined from high level ab initio molecular dynamics simulations. *J. Chem. Theory Comput.*, 8(10):3526–3535, 2012.

[152] E. Awoonor-Williams and C. N. Rowley. The hydration structure of methylthiolate from QM/MM molecular dynamics. *J. Chem. Phys.*, 149(4):045103, 2018.

[153] A. N. S. Adluri, J. N. Murphy, T. Tozer, and C. N. Rowley. Polarizable force

field with a σ-hole for liquid and aqueous bromomethane. *J. Phys. Chem. B*, 119(42):13422–13432, 2015.

[154] A. J. Hazel, E. T. Walters, C. N. Rowley, and J. C. Gumbart. Folding free energy landscapes of β-sheets with non-polarizable and polarizable CHARMM force fields. *J. Chem. Phys.*, 149(7):072317, 2018.

[155] J. Chowdhary, E. Harder, P. E. M. Lopes, L. Huang, A. D. MacKerell, Jr., and B. Roux. A polarizable force field of dipalmitoylphosphatidylcholine based on the classical Drude model for molecular dynamics simulations of lipids. *J. Phys. Chem. B*, 117(31):9142–9160, 2013.

[156] H. I. Ingólfsson, M. N. Melo, F. J. van Eerden, C. Arnarez, C. A. Lopez, T. A. Wassenaar, X. Periole, A. H. de Vries, D. P. Tieleman, and S. J. Marrink. Lipid organization of the plasma membrane. *J. Am. Chem. Soc.*, 136(41):14554–14559, 2014.